Wind Waves and Internal Waves in Base Mine Lake

by

David Lee Hurley

B.S., North Carolina State University 2013

A THESIS SUBMITTED IN PARTIAL FULFILLMENT OF
THE REQUIREMENTS FOR THE DEGREE OF

MASTER OF APPLIED SCIENCE

in

The Faculty of Graduate and Postdoctoral Studies

(Civil Engineering)

THE UNIVERSITY OF BRITISH COLUMBIA

(Vancouver)

August 2017

Abstract

Syncrude's Base Mine Lake is the first commercial scale demonstration of end pit lake technology in the Canadian Oil Sands. Following its commissioning in 2012 significant efforts have been made to monitor and understand its evolution. Of particular interest is the impact of surface and internal waves on the resuspension of fluid fine tailings and the effect of hydrocarbons on surface wind wave formation and growth. In this study the first complete description of the wind and internal waves in Base Mine Lake is presented.

Observations of surface wind waves were collected using two subsurface pressure gauges. Data revealed that wind waves in Base Mine Lake have short residence times and rarely generate bottom orbital velocities capable of resuspending fluid fine tailings. Additionally, numerical simulations of the wind waves in Base Mine Lake were performed with the SWAN model. Modeled wave heights were in good agreement with observations, and resuspension of fluid fine tailings was minimal even during the 10 year storm event.

As the surface of Base Mine Lake contains a hydrocarbon film its impact on surface wind waves was investigated in the laboratory and field. It was found that the hydrocarbon film dampens high frequency wind waves and results in a slower growing wind wave field dominated by longer wavelengths. Additionally, the presence of hydrocarbons also increases the critical wind speed needed to initiate wave growth. From these findings it is postulated that the hydrocarbon film on Base Mine Lake acts to decrease the fluxes of momentum, gas, and heat.

The internal waves in Base Mine Lake were simulated using Delft3D Flow. Simulated wave heights as large as 3 m were shown to oscillate for multiple days with little dampening, and despite the small surface area of Base Mine Lake (8 km^2) the internal waves were significantly influenced by the Coriolis force. This influence was seen in the form of simulated Kelvin and Poincaré waves which resulted in complex circulation patterns within the lake. The findings presented here provide a first picture into the impacts of waves on the reclamation of Base Mine Lake.

Lay Summary

Syncrude's Base Mine Lake is the first attempt at reclamation of a pit lake in the Canadian Oil Sands industry. Several lake features, such as increased amounts of sediment and decreased concentrations of oxygen in the water column, are currently slowing recovery efforts. These features are a result of mixing, which is often driven by surface wind waves and internal waves, waves that travel below the waters surface. In this study the surface and internal waves in Base Mine Lake were measured and modeled on a computer and in a laboratory. Results showed that surface waves led to minimal sediment resuspension and internal waves created complex lake circulations. Additionally, a surface oil film on Base Mine Lake slowed the growth and formation of surface wind waves. Ultimately, this research provides a first picture into the impacts of waves on pit lake reclamation.

Preface

This thesis presents the original research of the author, conducted under the supervision of Dr. Gregory Lawrence and Dr. Edmund Tedford. I performed the data collection of Chapter 2 and designed the laboratory and field experiments of Chapter 4 in collaboration with Dr. Tedford. I was solely responsible for the design and implementation of the numerical simulations in Chapters 3 and 5. A version of Chapter 4 has been submitted for publication as "Effects of Hydrocarbons on Wind Waves in a Mine Pit Lake" by D. Hurley, E. Tedford, and G. A. Lawrence. I was the lead investigator for the work presented in this chapter. E. Tedford assisted in the design and execution of laboratory and field experiments. I wrote the manuscript and my co-authors provided comments.

Table of Contents

Abstract ii

Lay Summary iii

Preface iv

Table of Contents v

List of Tables vii

List of Figures viii

List of Symbols x

Acknowledgments xii

1 Introduction 1
- 1.1 Study Site 2
- 1.2 Thermal Stratification 5
- 1.3 Wind Induced Processes 5
- 1.4 Thesis Motivation & Objectives 8
- 1.5 Thesis Outline 9

2 Measuring Wind Waves 10
- 2.1 Introduction 10
- 2.2 Subsurface Wave Properties 11
  - 2.2.1 Pressure Transfer Function 13
- 2.3 Data Collection 16
- 2.4 Results 18
  - 2.4.1 Nonlinearity 18
  - 2.4.2 Wave Environment 19

3 Modeling Wind Waves 23
3.1 Introduction 23
3.2 Model Setup 24
3.3 Results 26
3.3.1 Model Calibration 26
3.3.2 Model Validation 29
3.3.3 Resuspension 32
3.4 Conclusions 35

4 Effects of Hydrocarbons on Wind Waves 37
4.1 Introduction 37
4.2 Historical Background 38
4.3 Theoretical Background 38
4.4 Experimental Method 40
4.4.1 Laboratory 40
4.4.2 Field 41
4.5 Results 43
4.5.1 Laboratory 43
4.5.2 Field 46
4.6 Conclusions 48

5 Modeling Internal Waves 49
5.1 Introduction 49
5.2 Model Setup 50
5.2.1 Wind Drag Coefficient 51
5.3 Results 53
5.3.1 Rotational Effects 56
5.4 Conclusions 58

6 Conclusions 60
6.1 Summary 60
6.2 Impacts on Reclamation 63
6.3 Future Work 63

Bibliography 66

Appendices 72
Appendix A 72
Appendix B 74
Appendix C 76

List of Tables

Table 3.1 Comparison of simulated and observed wind waves: 2015 28
Table 3.2 Comparison of simulated and observed wind waves: 2016 31

Table 5.1 Comparison of simulated and observed isotherms . . . 53

Table B.1 SWAN parameters 74
Table B.2 Delft3D Flow parameters 75

List of Figures

Figure 1.1 Base Mine Lake map 4
Figure 1.2 Lake thermal stratification 6
Figure 1.3 Wind setup 8

Figure 2.1 Deep- and shallow-water waves 12
Figure 2.2 Pressure transfer function 14
Figure 2.3 Base Mine Lake bathymetry 17
Figure 2.4 Pressure sensor setup 18
Figure 2.5 Wave validity diagram 19
Figure 2.6 Observed wind waves: 2015 21
Figure 2.7 Observed wind waves: 2016 22

Figure 3.1 SWAN computational domain 25
Figure 3.2 Simulated wind waves: 2015 28
Figure 3.3 Simulated wind wave spectra: 2015 29
Figure 3.4 Simulated wind waves: 2016 30
Figure 3.5 Simulated wind wave fit: 2016 31
Figure 3.6 Simulated bottom orbital velocities 33
Figure 3.7 Forecast bottom orbital velocities 34
Figure 3.8 Simulated 10 year bottom orbital velocities 34

Figure 4.1 Dispersion relation 40
Figure 4.2 Laboratory setup 41
Figure 4.3 Field setup 42
Figure 4.4 Measured wind waves: Laboratory 44
Figure 4.5 Measure wind wave spectra: Laboratory 45
Figure 4.6 Measured wind waves: Field 47
Figure 4.7 Measured wavelengths: Field 47

Figure 5.1 Delft3D Z-model computational domain 51
Figure 5.2 Simulated and observed wind drag coefficient 52
Figure 5.3 Simulated isotherms 54

Figure 5.4 Simulated 17 ^{o}C isotherm 55
Figure 5.5 Simulated Kelvin and Poincaré waves 57
Figure 5.6 Simulated Coriolis effects 58

Figure A.1 Wind sensitivity analysis 72
Figure A.2 Wind Sandhill Fen Site 3 73

List of Symbols

C_d	Wind drag coefficient
c_o	Deep water wave speed
d	Depth of fluid
d_1	Depth of upper layer
DOY	Day Of Year
f	Coriolis parameter
f_s	Sampling frequency
f_c	Cutoff frequency
g	Gravitational acceleration
g'	Reduced gravitational acceleration
H	Wave height
H_s	Significant wave height
k	Wavenumber
K_z	Pressure transfer function
L_R	Rossby radius of deformation
m_n	Spectral moments
p	Absolute pressure
p_a	Atmospheric pressure
p_d	Dynamic pressure
p_g	Gauge pressure
S	Spectral energy
$S_{\eta\eta}$	Surface elevation spectrum
$S_{p_d p_d}$	Dynamic pressure spectrum
T	Wave period
Tm_{01}	Mean period
Tm_{02}	Average zero crossing period

T_R	Return period
T_P	Peak period
U^*	Momentum flux
U	Wind speed
U_b	Bottom orbital velocity
U_{bs}	Significant bottom orbital velocity
U_{Cr}	Critical bottom orbital velocity
W	Noise floor
z	Distance from free surface (- down)
η	Surface elevation
θ	Latitude
λ	Wavelength
ρ	Density of fluid
ρ_a	Density of air
ρ_1	Density of upper layer
ρ_2	Density of lower layer
σ	Surface tension
τ	Wind stress
ω	Wave angular frequency
Ω	Earths rotation rate

Acknowledgments

To my parents, Terry and Beverly. Despite the lighthearted heckling when I spent too much time in the mountains, I always received your unending support. I am forever grateful to the both of you.

My brother Matthew and friends Jack, Ming, Rory, and Will. Your encouragement of my wanderlust life was only exceeded by your unfaltering support when times were tough. Thanks!

To my grandmother, M. Metzger. Your interest in my work, encouraging attitude, and sense of humor always brightened my day.

A recognition to the National Sciences and Engineering Research Council of Canada (NSERC), Syncrude Canada Ltd., and the University of British Columbia for funding my studies.

Many thanks to my supervisor Dr. Gregory Lawrence and research associates Dr. Edmund "Ted" Tedford and Dr. Roger Pieters. You encouraged me to forge my own research and for that I am grateful.

A special mention to EFM group members Dr. Andrew Hamilton, Kelly Graves, Mark Sumka, and Sam Brenner for entertaining my questions and tolerating my quirks. Additional thanks to Co-op students Simon Fang and Jared Zhang for helping me prepare Chapter 4 for publication.

To all the folks at Syncrude Reclamation and Closure "Building 578". Your day in and day out cheerful moods, even in light of the Fort McMurray fires, were infectious. What a difference it made.

A very special thanks to Ted. Without your scientific curiosity and much welcomed insight this thesis would not be what it is now. I am extremely grateful for all the time you devoted to helping me succeed, and for being a great field partner even when the world was literally on fire.

Chapter 1

Introduction

The Canadian Oil Sands contain an estimated 166 billion barrels of recoverable oil, making it the third largest known oil reserves in the world (Government of Alberta, 2016 (retrieved August 3, 2017; Dompierre et al., 2017). However, unlike conventional oil reserves, where the oil deposits are found in subsurface reservoirs, the oil sands deposits are a below ground mixture of sand, water, and bitumen (Suncor, 2016 (retrieved August 3, 2017). Bitumen, a complex hydrocarbon with a viscosity approximately 100 times greater than blackstrap molasses, is extracted with surface and subsurface mining techniques (Strausz and Lown, 2003; Suncor, 2016 (retrieved August 3, 2017). Subsurface techniques, such as Steam Assisted Gravity Drainage (SAGD), use steam to heat the bitumen in situ so that it can then be pumped to the surface (Suncor, 2016 (retrieved August 3, 2017). Surface mining on the other hand requires the movement of oil sands from the ground to an extraction facility where hot water is used to strip the bitumen from the sands (Suncor, 2016 (retrieved August 3, 2017). Although less than 20% of all oil sands are recoverable via surface mining this technique has disrupted vast tracts of land and resulted in large quantities of mine byproducts, such as oil sands process affected water (OSPW) and fluid fine tailings (FFT) (COSIA, 2014 (retrieved August 3, 2017; Suncor, 2016 (retrieved August 3, 2017). In 2013 an estimated 900 km^2 of land had been disturbed by oil sands mining and less than 1% had been labeled as reclaimed (Dompierre et al., 2017). Additionally, the sheer volume of oil sands processed in extraction plants has resulted in more than $9.8x10^8$ m^3 of FFT, making it the world's largest deposit of tailings (COSIA, 2014 (retrieved August 3, 2017; Dompierre et al., 2017).

As laid out by the Alberta Energy Regulator, land disturbed by surface oil sands mining must be returned to an "equivalent capability" (Government of Alberta, 2016 (retrieved August 3, 2017). However, this mandated reclamation process is made more complex by several unique features of oil sands tailings. For one, FFT contain measurable concentrations of inorganic chemical constituents and organic compounds including residual bitumen (Dompierre et al., 2017). Additionally, the high water content of FFT,

initially no more than 35% solids by weight, results in low shear strengths which, due to the slow settlement and consolidation of the FFT, can persist well past the lifetime of a mine (COSIA, 2014 (retrieved August 3, 2017). To increase FFT shear strength, thereby allowing the FFT to be incorporated into terrestrial reclamation landscapes, a number of techniques to speed up settlement and consolidation rates have been put into practice. These include the addition of flocculants and coagulants, mechanical filtration, and large scale centrifugation (COSIA, 2014 (retrieved August 3, 2017). While these techniques are effective at dewatering FFT they are also prohibitively expensive and time consuming.

Instead an alternative reclamation strategy for oil sands tailings is to fill a mined out pit with FFT and cap it with a mixture of OSPW and non-process affected water. This effectively creates what is known as an end pit lake and is an attractive reclamation technique as it does not require the treatment of FFT before placement (CEMA, 2012 (retrieved August 3, 2017; Lawrence et al., 2016). The goal of an oil sands end pit lake is similar to that of a pit lake in the metal mining industry. They sequester material (FFT) to the bottom and treat process affected water (OSPW) in the water cap. Additionally, given enough time, they can be reincorporated into the natural hydrologic cycle (Pieters and Lawrence, 2014). However, unlike pit lakes in the metal mining industry, oil sands end pit lakes typically have thin water caps, generally less than 10 m, and the tailings, often FFT, have much finer particle sizes. In the future end pit lakes are expected to become an important aspect of the oil sands closure landscape. Currently there are more than thirty end pit lakes proposed in oil sands mine closure plans and all will be subject to reclamation requirements (Dompierre et al., 2017). This has motivated a need to understand the water cap physics of end pit lakes as the physical processes present in the water cap have implications on pit lake water quality and biology.

1.1 Study Site

Syncrude's Base Mine Lake (BML), located 40 km north of Fort McMurray Alberta, is the first commercial scale demonstration of an oil sands end pit lake (Figure 1.1A). The original mine pit, known as Base Mine, was decommissioned in 1994 and divided into an east-in pit and a west-in pit. From 1994 to 2012 the west-in pit was filled with FFT and capped with OSPW. As BML water was used in various mining processes during this period the water cap was maintained between 3 and 5 m thick. In 2012 the

filling of BML was stopped and the end pit lake was commissioned. At the time of commissioning the surface area of BML was approximately 8 km^2, the maximum FFT thickness was near 50 m, and the water cap was increased to an average depth of 8 m by pumping in non-process affected water from nearby Beaver Creek Reservoir (Figure 1.1B). Since commissioning the water cap has increased to a maximum depth of 11 m due to dewatering of the FFT. In general the nearshore areas of BML have steep to vertical bed slopes, an artifact of the mine pit. However, along the northern shoreline of BML a littoral zone, formed when the lake level was raised above the vegetation, is characterized by water depths less than 1.5 m. While this area consists of flooded vegetation, which naturally acts to reduce wave heights therefore minimizing sediment transport processes, a breakwater was still considered necessary. In result a rock breakwater was installed along the edge of the littoral zone to block surface waves (Figure 1.1B).

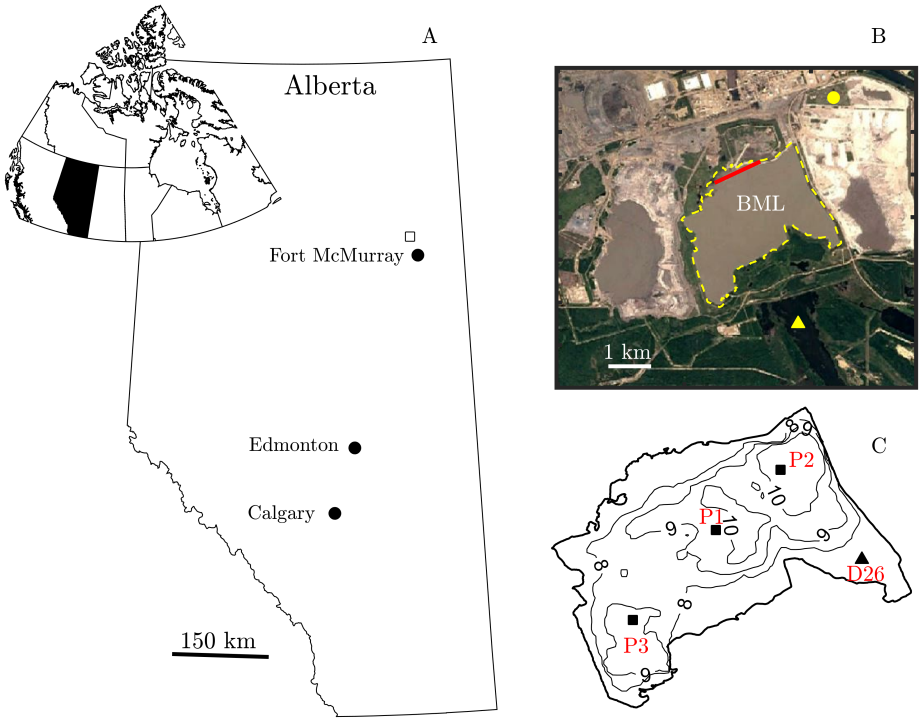

Figure 1.1: (A) Location of the province of Alberta within Canada. The location of the Syncrude Base Mine Site is indicated by the square in the zoom in of Alberta. (B) Satellite view of Syncrude's Base Mine with BML outlined in yellow. The yellow circle and triangle denote Sandhill Fen Site 3 and Beaver Creek Reservoir respectively. The rock breakwater is indicated by the red line. (C) Bathymetry of BML with the locations of the three platforms (P1,P2,P3) and the East Bay (D26) mooring.

Currently significant efforts are underway to understand the evolution of the physical limnology of BML. As a result, extensive measurements of water and atmospheric based variables are being taken. On the lake itself three platforms (P1, P2, P3) serve as the primary locations for the deployment of temperature, pressure, and turbidity moorings (Figure 1.1C). Additionally, an instrument mooring is regularly deployed in the East Bay (D26) of BML (Figure 1.1C). Water level measurements are taken at the southwest corner and surface wind waves are measured along the northeast embankment. Atmospheric variables such as wind speed, direction, and air pressure are

recorded on the lake at Platform 1 and off-site at Sandhill Fen Site 3 (Figure 1.1B,C).

1.2 Thermal Stratification

Lakes in the earth's mid-latitudes undergo significant temperature fluctuations with seasons (Wetzel, 1983). Under summertime heating the surface water becomes warmer than the bottom water and the lake becomes thermally stratified (Figure 1.2). Additionally, since density decreases with increasing temperature the surface water is less dense than the bottom water and therefore the stratification is stable. As the summer progresses the upper layers become more uniform in temperature and the thermal gradient sharpens. This area of sharpening is referred to as the thermocline and the waters above and below are known as the epilimnion and hypolimnion, respectively (Figure 1.2). As summer transitions into fall the surface water begins to cool and the thermal stratification weakens. Eventually, once the stratification is sufficiently weak, the lake will mix to a uniform temperature and thermal gradients will cease to exist (Figure 1.2). This process of mixing completely with depth is known as turnover.

With the onset of winter the surface water cools faster than the bottom water and results in a top heavy water column, dense water on top of less dense water. This thermally unstable stratification will persist until the bottom water reaches 4 ^{o}C, the temperature of maximum density. At that point the lake is once again thermally stable and the surface water may continue to cool below 4 ^{o}C leading to inverse thermal stratification (Figure 1.2). In some lakes, such as BML, an ice cover will form and the surface water will be kept just above the freezing temperature (Figure 1.2). In spring the surface layers will begin to warm towards the temperature of maximum density. Once the surface waters reach 4 ^{o}C the lake once again mixes completely with depth (Figure 1.2). Lakes that experience these turnover events twice per year are referred to as dimictic lakes.

1.3 Wind Induced Processes

In many lakes, including dimictic lakes, wind is the major driver of surface and subsurface motions. Initially the wind stress perturbs the lakes surface creating small ripples known as capillary waves (Kinsman, 1965). Assuming the fetch, speed, and duration of the wind is sufficient these waves will eventually grow into surface wind waves or gravity waves (Kinsman, 1965).

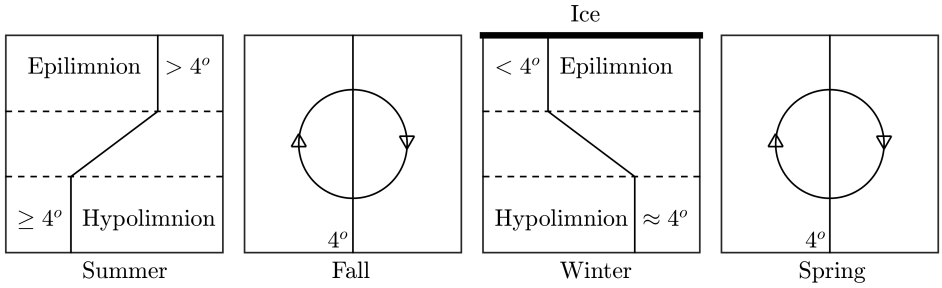

Figure 1.2: An idealized annual temperature cycle of a dimictic lake such as BML. The solid vertical line indicates the temperature profile in each season. The dashed horizontal lines denote the location of the epilimnion, thermocline, and hypolimnion. Fall and spring turnover is represented by the arrow inscribed circle.

In most cases the oscillating free surface elevation (η) associated with gravity waves is well approximated under linear (Airy) wave theory (Equation 1.1)(USACE, 1984).

$$\eta = \frac{H}{2}\cos(kx - \omega t) \tag{1.1}$$

Here H is wave height, k is wavenumber, and ω is wave angular frequency.

This theory, published by George Biddell Airy (1841), treats a propagating surface wave as a sinusoid and assumes the fluid is incompressible and inviscid, the flow is irrotational, and the free surface is uncontaminated. However, as the theory is linear and therefore neglects higher order nonlinear terms, its use is generally limited to waves propagating in water depths much greater than their wavelength. Following Airy's theory a number of nonlinear wave theories were proposed to account for nonlinear effects on a propagating wave. These include solitary, Stoke's, cnoidal, and numerical wave theories (Stokes, 1847; Boussinesq, 1871; Wiegel, 1960). Of these, Stokes' second order nonlinear wave theory has been widely applied to surface waves in deep water and has been shown to better reproduce the free surface elevation of a wave train (USACE, 1984). In this case the oscillating free surface is no longer sinusoidal and instead the wave troughs become elongated and the crests become compressed (Equation 1.2).

$$\eta = \frac{H}{2}\cos(kx-\omega t)+\left(\frac{kH^2}{16}\right)\frac{\cosh(kd)}{\sinh^3(kd)}(2+\cosh(2kd))\cos(2kx-2\omega t) \tag{1.2}$$

Along with surface wind waves a wind stress on the free surface creates a surface setup or a piling of water at the downwind end (Figure 1.3A) (Stevens and Lawrence, 1997). In the most basic sense this setup can be represented by a linearly sloped free surface which becomes steeper the greater the wind speed (Equation 1.3) (Monismith, 1987; Stevens and Lawrence, 1997). Furthermore, if the lake is thermally stratified the surface setup will result in an opposite setup of the thermocline (Figure 1.3A) (Stevens and Lawrence, 1997). However, while the surface setup is generally on the order of millimeters the magnitude of the internal setup can be a thousand times larger (Mortimer, 1952). This is because the density difference across the thermocline is much smaller than the density difference across the air-water interface (Equation 1.4)(Stevens and Lawrence, 1997; Mortimer, 1952).

$$\frac{dd}{dx} = \frac{\tau}{\rho_1 g d_1} \tag{1.3}$$

$$\frac{dd_1}{dx} = \frac{\tau}{\rho_1 g' d_1} \tag{1.4}$$

$$g' = \frac{\rho_2 - \rho_1}{\rho_2} g \tag{1.5}$$

Where d is fluid depth, τ is wind stress, ρ_1 and ρ_2 are fluid density above and below the thermocline respectively, g is local gravitational acceleration, d_1 is depth of upper layer, and g' is reduced gravity.

Once the wind relaxes the surface and internal setups will begin to oscillate back towards equilibrium (Figure 1.3B). As a result internal waves, gravity waves propagating along the thermocline, are generated. These waves are similar to surface gravity waves, but due to the reduced density gradient across the thermocline their amplitudes are much larger and wave speeds much slower (Mortimer, 1952). The dominant internal waves often have wavelengths comparable to or larger than the length of the lake. When this is the case the waves are capable of reflecting back and forth between the basin walls without appreciable damping. This oscillation is generally referred to as an internal or baroclinic seiche (Mortimer, 1952). These seiche events generate strong horizontal velocities above and below the thermocline, a result of large wave amplitudes and wavelengths (Mortimer, 1952). Additionally the seiche generated velocities are a maximum when the deflection of the thermocline from equilibrium is at a minimum and vice versa (Figure 1.3B)(Mortimer, 1952).

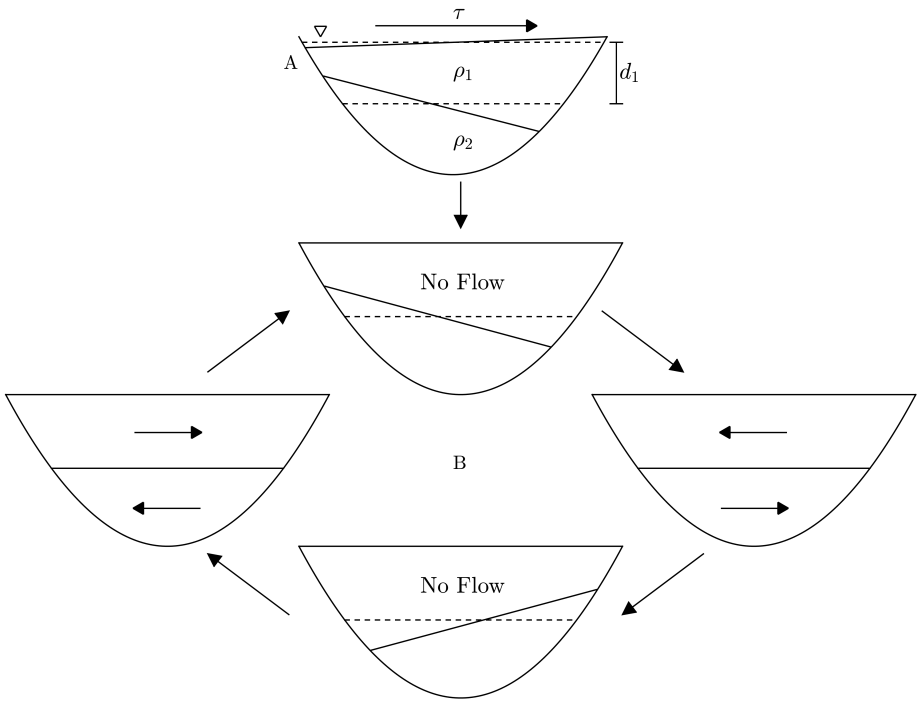

Figure 1.3: (A) Idealized surface and internal setup for a two layer lake resulting from a wind stress. The equilibrium position for the surface and thermocline are indicated by the dashed line. (B) Oscillation of the thermocline in the absence of wind. The oscillation of the free surface is quickly dampened and therefore not shown. The direction of the horizontal velocities in the epilimnion and hypolimnion are denoted by arrows.

1.4 Thesis Motivation & Objectives

Both surface and internal waves play important roles in driving mixing in lakes. Oscillating motions, known as orbital velocities, occur beneath wave crests and troughs creating localized shear stresses. In nearshore areas surface and internal waves break and generate turbulent motions that can extend the depth of the water column. Additionally, internal waves can generate significant circulation patterns at depth and surface waves can enhance nearshore currents as a result of refraction and reflection. At the air water interface whitecapping of surface wind waves and upwelling and downwelling associated with internal waves can enhance the fluxes of gas and heat.

The aim of this research is to provide the first description of the wind and internal waves in Base Mine Lake through field measurements, laboratory experiments, and numerical simulations. The goal is that this initial picture will help elucidate the impact of wave dependent mixing mechanisms on the water cap physics and subsequently inform future reclamation decisions. Of particular interest in this study is the consequence of wave generated bottom orbital velocities on the resuspension of FFT and the effect of surface hydrocarbons on wind waves.

1.5 Thesis Outline

This thesis is divided into six distinct chapters. Chapter 1 provides an introduction to the research along with the motivation for it. This includes an overview of Oil Sands end pit lakes, a description of Base Mine Lake, and a brief literature review on lake stratification, wind waves, and internal waves. Chapter 2 presents the observed wind waves in Base Mine Lake. In addition, the instrument setup is described and the challenges associated with measuring wind waves in small lakes is addressed. Chapter 3 discusses the setup of the SWAN model and displays the model resultant wind waves. The modeled and observed wind wave induced resuspension of FFT is also discussed. Chapter 4 looks to quantify the effect of hydrocarbons on wind waves through field and laboratory experiments. Chapter 5 compares the observed internal waves to the modeled internal waves from Delft3D Flow. Additionally, the effects of rotation and the parameterization of the wind drag coefficient is examined. Lastly, Chapter 6 provides a concluding summary of the research, some implications of the findings on reclamation of BML, and suggestions for future work.

Chapter 2

Measuring Wind Waves

2.1 Introduction

Measuring the properties of short period wind waves ($\omega > 0.25$ Hz), such as those found in many inland water bodies, is a non-trivial task. Typically wave parameters such as wave height and wavelength are estimated from either direct or indirect measurements of the surface elevation. In the case of direct measurements the real surface elevation is recorded using instruments such as surface piercing gauges, wave-rider buoys, and ultrasonic probes. However, as most of these instruments are designed for oceanic environments they typically sample too infrequently and have too coarse a spatial resolution to resolve high frequency small amplitude wind waves (Hasselmann et al., 1973). Instruments that measure the surface elevation indirectly, through a related property such as pressure or velocity, are potentially capable of sampling fast enough to resolve high frequency waves. Though, unlike direct measurements, indirect measurements require the application of a transfer function to convert the related property to a surface elevation signal (USACE, 1984). This conversion is generally done by applying linear and in some cases nonlinear wave theory (USACE, 1984).

Numerous studies have shown that linear wave theory can adequately transform pressure to surface elevation for long period (Bishop and Donelan, 1987; Townsend and Fenton, 1997; Tsai et al., 2005) and in some cases short period waves (Jones and Monismith, 2007). Additionally, this application has been shown to be successful in the presence (Gabriel and Hedges, 1986; Jones and Monismith, 2007) and absence of a mean flow. However, as the frequency of the waves increase, the instrument noise can begin to dominate the signal and lead to inaccurate estimates of a wave's properties. Attempts to minimize this error by using higher order nonlinear wave theories have been made with marginal success (Townsend and Fenton, 1997; Oliveras et al., 2012). Some studies have even looked into the use of empirically derived transfer functions to more accurately ascertain the surface elevation signal, again with mixed results (Wang et al., 1986; Tsai et al., 2002). Instead Jones and Monismith (2007) found that by identifying the frequency

of the waves of interest beforehand, the instrument sampling rate (f_s) and deployment depth could be chosen such that linear wave theory was able to reasonably resolve the surface elevation of small amplitude high frequency waves.

The purpose of this chapter is to examine the use of pressure sensors for measuring high frequency wind waves in BML. Measurements were collected using two pressures sensors, sampling at different rates, during various periods in the fall of 2015 and 2016. First the subsurface wave properties are discussed, and the equation for subsurface pressure, assuming linear wave theory, is given. Then the challenges and consequences of applying linear wave theory to convert pressure signals generated by small amplitude high frequency waves to surface elevations is addressed. Lastly the details of the field campaign and the first ever observations of wind waves in BML are presented.

2.2 Subsurface Wave Properties

A common way to classify surface waves is by their relative depth (d/λ), a ratio of the depth (d) in which they travel to their wavelength (λ) (Kinsman, 1965; USACE, 1984). Shallow-water waves have wavelengths much longer than the depth ($\lambda > 20d$) and subsurface velocities, herein referred to as orbital velocities, that move in elliptical paths (Figure 2.1A). Deep-water waves have wavelengths less than twice the depth ($\lambda < 2d$) and orbital velocities that move in circular paths (Figure 2.1B). In shallow water the orbital velocities decay minimally with depth, while in deep water they decay exponentially with depth and are negligible at the seabed. Similarly, the wave generated subsurface pressure, herein referred to as dynamic pressure, follows the same decay with depth. To better understand the decay in amplitude of dynamic pressure with depth the linear wave theory equation for subsurface pressure, herein referred to as gauge pressure, is examined.

In the presence of surface waves gauge pressure, $p_g = p - p_a$, where p is absolute pressure and p_a is atmospheric pressure, contains a static and a dynamic component (Equation 2.1). The static component, first term in Equation 2.1, increases linearly with depth. While the dynamic component, second term in Equation 2.1, is a result of the oscillating free surface (Equation 2.2). As the amplitude of the dynamic component, p_d, measured at a given depth, may have decayed, a pressure transfer function, K_z, is needed to retrieve the surface amplitude (Equation 2.3).

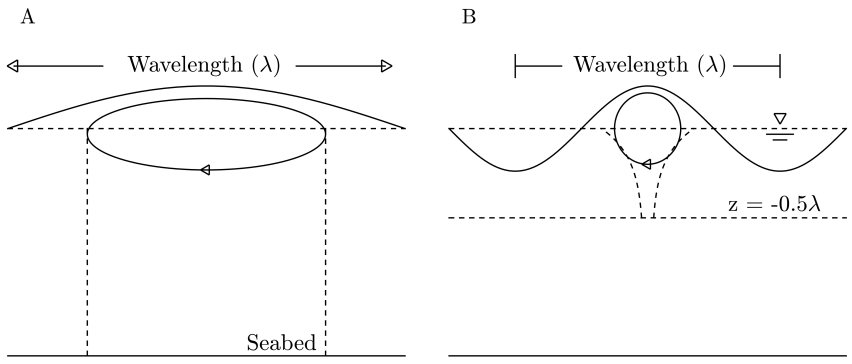

Figure 2.1: Orbital velocities due to the deflection of the free surface from the mean water level for (A) shallow-water and (B) deep-water waves. The magnitude of the velocities becomes negligible in deep water at a distance of half a wavelength below the free surface (z) (B).

$$p_g = -\rho g z + \rho g \eta K_z \tag{2.1}$$

$$p_d = \rho g \eta K_z \tag{2.2}$$

$$K_z(z) = \frac{\cosh(2\pi(z+d)/\lambda)}{\cosh(2\pi d/\lambda)} \tag{2.3}$$

Where z is the distance from the free surface (negative is downwards) and η is the surface elevation.

For a constant fluid depth, K_z is a function of wavelength. In shallow-water, when wavelength is much larger than the depth, the value of K_z at any distance below the free surface is approximately 1 (Equation 2.3). This results in dynamic pressure signals at the surface and the seabed that are equal. In deep water, when depth is much larger than wavelength, the expression for K_z tends to $e^{2\pi z \lambda^{-1}}$. Therefore, the amplitude of the dynamic pressure decays exponentially with increasing distance below the free surface. Furthermore, at a distance of half a wavelength below the free surface, when $K_z = e^{-\pi}$, the amplitude of the dynamic pressure will have decayed to negligible values (Figure 2.1B). This means that a pressure sensor positioned deeper than half a wavelength below a deep-water wave would sense primarily the hydrostatic pressure.

2.2.1 Pressure Transfer Function

Given a dynamic pressure signal the surface elevation can be found by rearranging Equation 2.2. This can be done in time or frequency space. In time space the wavelength of each individual wave in the time series of dynamic pressure is found using the zero up-crossing method (USACE, 1984). Then a value of K_z can be determined for each wave in the record and applied to Equation 2.2. This results in an estimate of the surface elevation. However, errors introduced during the zero up-crossing method and an incomplete estimate of K_z across the wind wave spectrum may be problematic. Instead, a preferred method is to perform a spectral analysis on the dynamic pressure signal, calculate K_z for a range of frequencies, and transform the dynamic pressure spectrum to a surface elevation spectrum (Equation 2.4). Once the surface elevation spectrum is known the associated significant wave height (H_s), the mean of the highest one-third of waves, can be determined from the spectral moments (Equation 2.6). Additionally, the surface elevation spectrum can be transformed into a surface elevation time series by mapping the frequencies back to time space.

$$S_{\eta\eta}(\omega) = \frac{S_{p_d p_d}(\omega)}{K_z^2} \tag{2.4}$$

$$m_n = \int_0^\infty \omega^n S_{\eta\eta}(\omega) d\omega \tag{2.5}$$

$$H_s = 4\sqrt{m_0} \tag{2.6}$$

Where $S_{\eta\eta}$ is the surface elevation spectrum, $S_{p_d p_d}$ is the dynamic pressure spectrum, ω is wave angular frequency, m_n is the spectral moments, and m_0 is the zeroth spectral moment or variance of the surface elevation signal.

Noise Amplification

The sources of noise in a subsurface pressure signal can be hard to pinpoint. Environmental factors such as turbulence and biofouling, and mechanical imperfections such as vibrations from the power system lead to a nonzero noise floor in all subsurface pressure gauges. At high frequencies the dynamic pressure signal approaches the noise floor (W) and the pressure transfer function, K_z, tends towards zero (Figure 2.2A). This means a significant amount of energy (S) in the dynamic pressure spectrum at high

frequencies is due to noise. As a result there is an overamplification of energy in this frequency range via Equation 2.4, and an overestimation of the high frequency surface elevations and the significant wave height (Figure 2.2B). This is especially apparent during calm periods as the wave energy is concentrated at higher frequencies and decays exponentially with depth so that the dynamic pressure spectrum falls below the noise floor a short distance beneath the free surface.

A number of techniques have been proposed to deal with the overamplification of high frequency noise. The simplest solution is to analyze only storm events, when the peak in the frequency spectrum is clearly discernible and centered at low frequencies (Figure 2.2A). However, even then an overamplification of noise at high frequencies will occur (Figure 2.2B). Another option would be to move the subsurface pressure gauge closer to the free surface, thereby reducing the amount of decay in the dynamic pressure signal. This would increase resolution in the spectrum at high frequencies, but as the sensor may come out of the water in large waves it would fail to capture storm events. The best solution would be to use multiple subsurface pressure gauges, with high sampling rates, positioned at various depths. This way each sensor would resolve a specific frequency band and the array as a whole would capture a more complete picture of the dynamic pressure spectrum (Jones and Monismith, 2007).

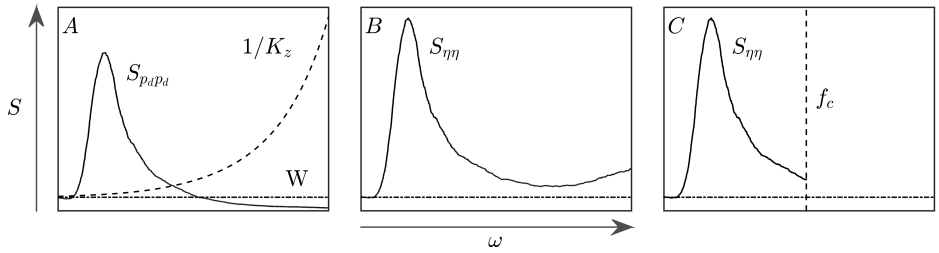

Figure 2.2: Dynamic pressure spectrum ($S_{p_d p_d}$) with the pressure transfer function (K_z) shown as a multiplier and the instrument noise floor (W) indicated (A). The estimated surface elevation spectrum ($S_{\eta\eta}$) from Equation 2.4 (B). Surface elevation spectrum after removing overamplified noise with a cutoff frequency (f_c) (C).

As an array of pressure sensors is generally impractical a more typical way to deal with overamplified noise is through filtering. One method is to remove the noise floor before applying the pressure transfer function. Though in practice, identifying noise due too environmental sources is ex-

tremely difficult. Instead, a more common technique is to choose a high frequency cutoff (f_c) and apply a low-pass filter. As there is no automated technique for choosing the cutoff frequency, it is typically chosen as a point where the energy from the dynamic pressure signal is well above the noise floor. This effectively removes the overamplified noise, though it comes at the cost of losing spectral resolution (Figure 2.2C). However, if the wave energy beyond the cutoff frequency is negligible, such as in a storm event, then little error will be introduced into the estimation of the surface elevations and significant wave heights.

Nonlinearity

In applying the pressure transfer function to the dynamic pressure spectrum for deep-water waves ($K_z \neq 1$), the resulting wave heights (H) in the surface elevation signal are larger than those found in the dynamic pressure signal. However, the wavelengths in the surface elevation signal are identical to those in the dynamic pressure signal. This consequently leads to an artificial steepening of the waves towards the breaking limit (Equation 2.7).

$$\frac{H}{\lambda} > \frac{1}{7} \tag{2.7}$$

As the waves approach the breaking limit they become more nonlinear. Generally this nonlinearity can be minimized with the choice of the cutoff frequency. Regardless, an assessment of the nonlinearity resulting from the application of the pressure transfer function is needed to 1) determine if there are waves exceeding the breaking limit and 2) quantify the error introduced by using the linear wave theory equation for dynamic pressure instead of a nonlinear theory.

To accomplish this the height and period of every wave in the surface elevation time series is extracted using the zero up-crossing method (USACE, 1984). The wave field can then be mapped onto the wave validity diagram of Le Méhauté and Koh (1967). This provides guidance as to what wave theory (linear or nonlinear) best explains the measured signal and shows the percentage of waves that exceed the breaking limit. It is worth noting that the wave validity diagram provides an approximation as to where linear wave theory ends and nonlinear theories begin as the regime lines are not formal.

2.3 Data Collection

Measurements of the wind waves in BML were collected using two subsurface pressure sensors from October 6-28 2015 and August 15 to October 19 2016. Each sensor was mounted to a steel piling (2" ND) that was located in 3 m of water and positioned 8.2 m from the shoreline (Figure 2.3). During the 2015 campaign a single RBR Duo sampling continuously at 6 Hz was positioned 2.75 m above the lake bed (Figure 2.4). In 2016 an RBR Solo sampling continuously at 16 Hz and positioned 2.9 m above the lake bed was added (Figure 2.4).

The shallow mounting of the instruments meant it was possible for them to come above the free surface during large wave events. As a result the instruments were oriented downward to reduce the potential for surface contaminants to become trapped on the sensor faces post event. The published accuracy of both sensors is 0.05% of the full scale and the resolution is better than 0.001% of the full scale. Every three weeks the instruments were removed, serviced, and redeployed in less than twenty-four hours.

Post deployment it was found that both sensors had recorded subsurface pressures to be less than atmospheric. To address this a constant pressure offset for each instrument was found by taking the average of the difference between the recorded out of water pressure and the atmospheric pressure during a 15 minute period. This offset was found to be +0.36 dbar and +0.40 dbar for the 6 Hz and 16 Hz sensors, respectively. Additionally, a phase shift and a spurious signal, occurring once a minute, in the 6 Hz sensor was corrected. The dynamic pressure signal (Equation 2.2) was found by removing the atmospheric and hydrostatic pressure components from the raw subsurface pressure (p). All data (pressure, water elevation, etc.) were oversampled to 16 Hz to aid with post-processing.

Spectral analysis of the dynamic pressure was performed by dividing the signal into rectangular windows and performing a fast Fourier transform. In 2015 only the storm events were analyzed (see section 2.2.1) with the window length set to the storm length. However, in 2016, with the addition of better deployment protocols, the signal was split into 10 minute windows. In each window a high-pass filter was applied to remove the baratropic waves ($\omega < 0.1Hz$) and the average depth of the sensor face below the free surface was computed. Then the pressure transfer function (Equation 2.3) was calculated for each window.

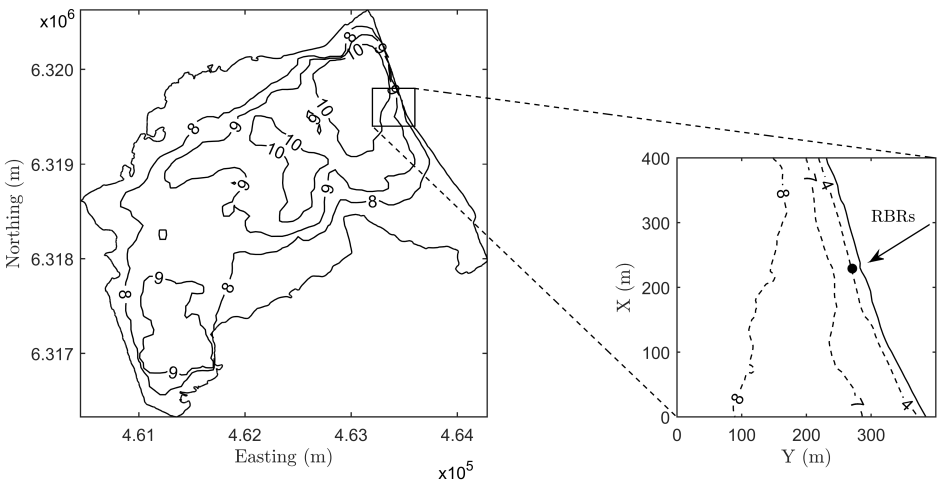

Figure 2.3: Map of BML with contoured depth in meters and the location of the steel piling with the mounted RBR sensors inset.

Lastly, the dynamic pressure spectrum was transformed into a surface elevation spectrum (Equation 2.4) and a low-pass filter with cutoff frequencies of 1.3 Hz for the 6 Hz sensor and 2 Hz for the 16 Hz sensor was applied. In addition to reasons discussed in section 2.2.1, these cutoff frequencies were chosen with the instrument depth below the free surface in mind. For example, a 2 Hz wave will have a wavelength of approximately 40 cm. This means that 10 cm below the free surface, the location of the 16 Hz sensor, the dynamic pressure associated with a 2 Hz wave will have decayed by a factor of five (Equation 2.3). Therefore, despite a Nyquist frequency ($f_s/2$) of 8 Hz, the 16 Hz sensor was considered unreliable above 2 Hz based on the sensor depth alone. After filtering, the surface elevation spectrum was mapped back into a surface elevation time series by performing an inverse fast Fourier transform. The standard deviation of the surface elevation in each window was then calculated and the significant wave height was computed by applying Equation 2.6.

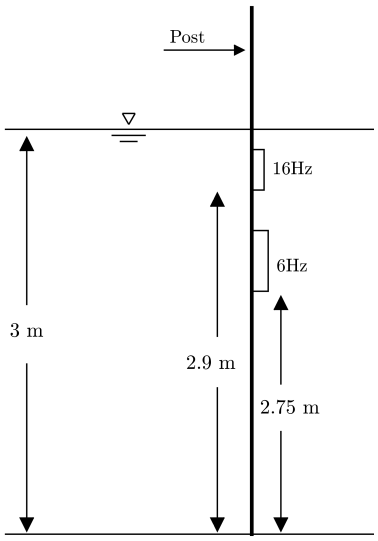

Figure 2.4: Schematic of the instrument setup. The fluid depth is from the lake bed to the mean water level and instrument heights are from the lake bed to the sensor face.

2.4 Results

2.4.1 Nonlinearity

After estimating the surface elevation the nonlinearity of the resulting waves was assessed in order to determine the validity of the measurements (see 2.2.1). Figure 2.5 showcases the characteristics of the wave properties from six distinct storm events during the 2015 campaign. During these storms the waves were primarily deep-water waves and exhibited mostly nonlinear characteristics. However, none of the waves during these periods exceeded the breaking limit. Additionally, the ratio of the linear dynamic pressure to the Stokes second order dynamic pressure (USACE, 1984) is shown as a percent error. As expected the closer you get to the breaking limit the steeper and more nonlinear the waves become and the more error you incur by assuming a linear equation. Despite this the maximum error is 4%, indicating that linear theory is a safe assumption even when nonlinear waves exist. Ultimately this means that the difference between the estimated surface elevations using linear and nonlinear theories is also less than 4%.

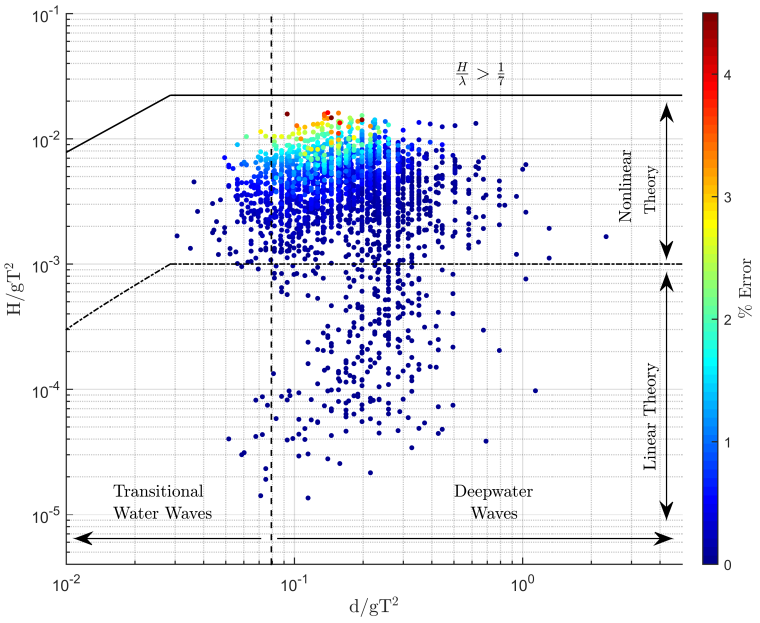

Figure 2.5: The wave validity diagram of Le Méhauté and Koh (1967) with the wave properties from six storm events in 2015 shown as dots. Deep-water and transitional-water waves, separated by the vertical dashed line, are divided into linear and nonlinear wave regimes. The breaking limit is indicated by the topmost line. The ratio of the linear dynamic pressure to the Stokes second order nonlinear dynamic pressure (USACE, 1984) is indicated as a percent error.

2.4.2 Wave Environment

The observed wind waves and meteorological conditions on BML for the 2015 and 2016 campaigns are shown in Figure 2.6 and Figure 2.7, respectively. All dates from this point forward are displayed as day of year (DOY) where day of year 1.5 is January 1 at noon. During both years, winds greater than 5 m/s were predominately from the southwest through northwest quadrant, and to a lesser extent from the north (Figure A.2). The westerly winds were aligned with the longest fetch to the instruments and produced the largest waves at the sensors (Figure 2.6, 2.7). This was the case even when the wind speed during a westerly was slower than non-westerly periods, as shown in box *ii* of Figure 2.7. The short fetch from the eastern shoreline to the instruments meant that winds from the southeast through northeast

produced only small waves at the sensors, regardless of wind speed. This is readily visible in shaded region *i* of Figure 2.7.

In 2015 there were six distinct storm events (a-f) that produced waves with a peak period of approximately 2 s and significant wave heights ranging from 5 to 38 cm (Figure 2.6). The maximum wave height in the record occurred during storm *a* and was approximately 60 cm which corresponds to a significant wave height of approximately 38 cm (Figure 2.6A). In comparison the theoretical fetch limited significant wave height and peak period (USACE, 1984), using the maximum observed wind speed of 12 m/s and a fetch of 3 km, is 33 cm at 2 s. As described in detail in section 2.2.1 and section 2.3 only the storm events were analyzed leading to exaggerated calm periods in the remainder of the record. One feature of particular interest is the three hour calm period between storms *b* and *c* (Figure 2.6A). It is likely that there was a shift in the wind direction, a relaxation of the wind speed, or both that was too fine to be resolved by hourly average wind parameters. Additionally, this shows that unlike larger bodies of water where wind waves and swell can exist for days or weeks the waves in BML quickly dissipate.

During the 2016 campaign the wind waves had a peak period of 2 s and significant wave heights that ranged from 0 to 30 cm with a maximum wave height of approximately 70 cm (Figure 2.7). Both the 6 Hz and 16 Hz sensors showed similar wave heights with only minor variations due primarily to differences in instrument depths (Figure 2.7A,B). In large wave events, box *i* Figure 2.7A, the proximity of the 16 Hz sensor to the free surface meant it came out of the water, notice the wave troughs are much smaller than the wave crests. There are also more small amplitude wave events in the 2016 record (Figure 2.7A,B) than in the 2015 record (Figure 2.6A). This is an artifact of better data processing and shallower instrument deployments (see section 2.3).

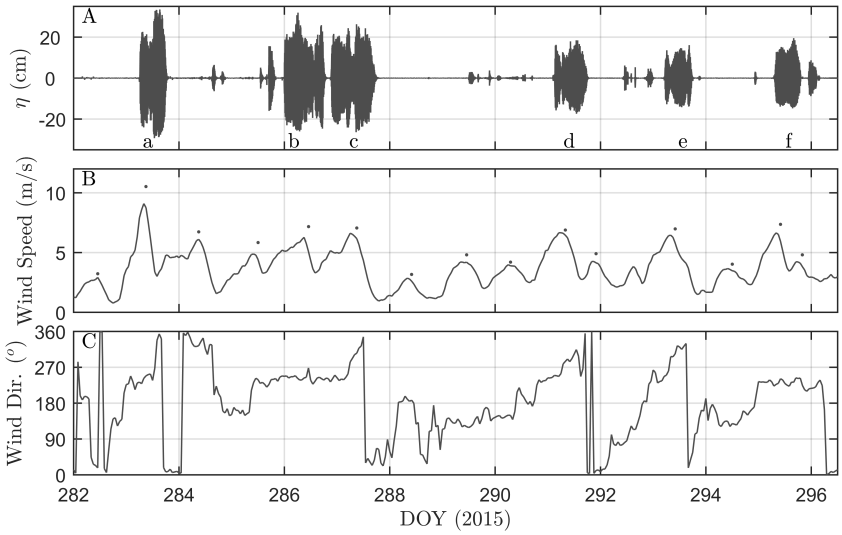

Figure 2.6: The estimated estimated surface elevation (A) showing six distinct storm events (a-f). Measurements of the hourly average and daily maximum (·) wind speed (B) and direction (C) at Sandhill Fen Site 3 (see Figure 1.1)

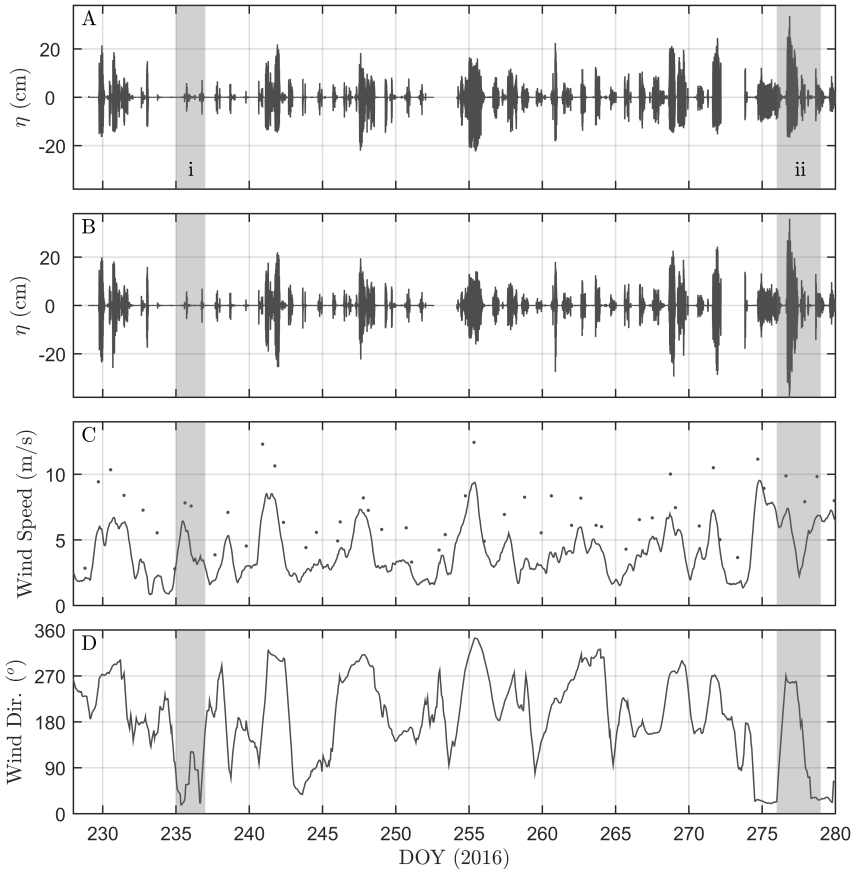

Figure 2.7: The estimated surface elevations from the 16 Hz (A) and 6 Hz (B) sensors. Measurements of the hourly average and maximum (·) wind speed (C) and direction (D) at Sandhill Fen Site 3 (see Figure 1.1). The grey boxes indicate features of interest. Notice that the 16 Hz sensor comes out of the water during large wave events (ii). Easterly winds fail to generate waves at the sensors (i) while westerly winds, even at relatively slower wind speeds, generate the largest waves due to the large fetch (ii).

Chapter 3

Modeling Wind Waves

3.1 Introduction

In order to elucidate the role of wind generated surface waves on physical processes, such as sediment resuspension and shoreline erosion, a description of the wind wave field beyond a point measurement is critical. Often this is accomplished in one of two ways. The first, and most basic way, is to estimate significant wave heights and associated peak periods with a one dimensional fetch based model. Typically, due to the complexity of the wind wave processes, these models are based on semi-empirical relationships (Ozeren and Wren, 2009). This has resulted in numerous field studies conducted in ocean (Hasselmann et al., 1973) and coastal (Sverdrup and Munk, 1947; Bretschneider and Reid, 1954) environments as well as large (Schwab et al., 1984) and small (Ozeren and Wren, 2009) inland water bodies to determine the relation between wave growth and the wind. However, as these models are a function of only wind speed, duration, and fetch they don't account for the effects of shallow water processes and bathymetry on the surface waves.

Instead, a more complete picture can be achieved with a third generation wave model. These models simulate the wind wave field by solving the spectral action balance equation allowing the two dimensional wave spectra to evolve without constraints on spectrum shape or energy (Tolman and Chalikov, 1996). Among the many third generation wave models available the most widely used are SWAN (Simulating WAves Nearshore), WAM (WAve Model), and WaveWatch III. SWAN, developed for coastal applications, simulates wave parameters at a high spatial and temporal resolution, accounts for shallow water processes such as diffraction, refraction, shoaling, and breaking, and allows for spatially varying winds (Booij et al., 1999). SWAN has been applied and validated in coastal areas (Booij et al., 1999), bays of complex geometry (Lowe et al., 2005; Hoeke et al., 2011) large lakes (Jin and Ji, 2001), and estuaries in the presence and absence of a mean flow (Gorman and Neilson, 1999).

While some studies have used SWAN to simulate waves in small bodies of water (Seibt et al., 2013) it has generally been assumed that one dimen-

sional fetch based models are sufficient. However, a recent study by Seibt et al. (2013) showed that SWAN more closely matched the observed wave field in the nearshore zone of a medium sized lake when compared to a fetch based model. In the nearshore zone sediment resuspension is heavily influenced by surface wave induced motions at the bed (Lawrence et al., 1991; Wiberg and Sherwood, 2008). These motions, known as a waves bottom orbital velocity, are directly proportional to wave height and dependent on wave period (Lawrence et al., 1991; Wiberg and Sherwood, 2008). While bottom orbital velocities can be estimated from statistical wave parameters, such as significant wave height and peak period, it has been shown that estimates using the full wave spectrum are more accurate (Wiberg and Sherwood, 2008). Therefore, as fetch based models do not resolve the full wave spectrum and can lead to inaccurate estimates of wave heights in the nearshore zone a third generation wave model such as SWAN is preferred when estimating resuspension rates at various depths.

In this chapter the wind waves on BML are simulated in SWAN and compared to the wave observations from the 2015 and 2016 sampling periods. First the model setup is described and then the results of the simulations are presented. Next, the model predicted sediment resuspension is compared with an estimate of resuspension based on the observed wave field. Then the model estimated sediment resuspension at all depths in BML during two wave events is shown. Lastly, the general findings and implications of the wind waves on sediment resuspension are discussed.

3.2 Model Setup

The SWAN model, incorporated into Delft3D (WL—Delft Hydraulics), was calibrated to BML during the October 9-23 2015 sampling period and validated during the August 16 to October 14 2016 sampling period. In both periods the wind waves were simulated on a computational domain covering the extent of BML and consisting of a rectangular grid with a resolution of 50 $\times$ 50 m (Figure 3.1). Additionally a nested domain with a resolution of 5 $\times$ 5 m extending outwards from the location of the RBR pressure sensors helped resolve the nearshore wave properties (Figure 3.1). Model bathymetry was interpolated from single beam sonar data with 2 m resolution to the computational and nested domains. Since SWAN models the waves as an evolving two-dimensional wave spectrum the spectral resolution in frequency and direction space must be predefined. In this study SWAN was prescribed 72 frequency bins ranging from 0.25 to 3 Hz and 36 direc-

tional bins with constant 10 degree spacing. This spectral resolution was found to provide the best fit in the 2015 calibration period. Additionally, the frequency resolution extended to higher values compared to other studies as the wind waves in small lakes have shorter periods than those in coastal environments.

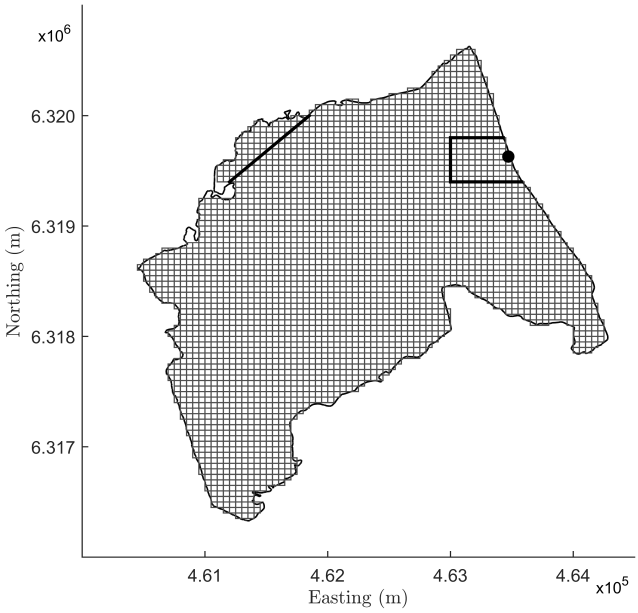

Figure 3.1: The computational domain for BML with the boundaries of the nested domain denoted by the three sided box and the location of the RBR's indicated by the black dot. The thick line along the northern boundary denotes the location of the littoral zone parameterized in SWAN.

During the 2015 and 2016 simulations the model was run with a time step of 60 minutes and forced with hourly average wind speed and direction recorded at Sandhill Fen Site 3. In both years the computational domain was prescribed a constant wind field which was justified given the small surface area of BML. Additionally, as Sandhill Fen Site 3 is located approximately 1.5 km from the lake a sensitivity analysis between the BML Central Platform and the Sandhill Fen site was carried out (Figure A.1). It was found that in general there is little difference between the two meteorological stations. The effects of a littoral zone and a submerged breakwater on the waves was parameterized in SWAN (Figure 3.1). This was done by prescribing a line of grid cells in which the waves would be allowed to transmit

no more than 50% of their energy across. Additionally, the flux of wave energy across the boundaries and reflections at the boundaries were considered to be zero. During the 2015 simulation the model value for diffraction was calibrated while all other parameters were left as default (Table B.1). The model output of significant wave height, peak period, significant bottom orbital velocity, and 1D wave spectra at the location of the RBR pressure sensors was recorded hourly.

Computational Mode

Within SWAN a simulation can be performed in the stationary or non-stationary mode. In the stationary mode the time derivatives are dropped from the spectral action balance equation and the model solution converges to a steady state in every time step (SWAN Team et al., 2011). The non-stationary, or quasi-stationary mode, does not ignore the time derivatives so that the model solution at each time step is a function of the previous time steps solution. In other words a stationary model predicts a wave field similar to that of a fetch limited model while a quasi-stationary model does not.

The decision to use the stationary or nonstationary mode depends on a number of factors. One consideration is that if the time needed for a wave to propagate through the computational domain is much less than the timescale on which the wind changes then the stationary mode can be chosen. It has been found that in general when the domain is less than 100 km then the stationary mode assumption is valid (SWAN Team et al., 2011). In all other cases the nonstationary mode is necessary. For this study the SWAN simulations were always performed in the stationary mode.

3.3 Results

3.3.1 Model Calibration

Comparison of the simulated and observed hourly significant wave heights during the 2015 sampling period are shown in Figure 3.2A. The SWAN simulation reproduces the timing and height of the observed wind waves during the six storm events (a-f) with reasonable accuracy. This is especially true when the wave heights during an event have a distinct maximum (Figure 3.2A a,d-f). In more complicated events, when there are multiple local maximums in the wave height, the model begins to deviate from the observations (Figure 3.2A b,c). Notice that the rate of change of the model wave heights

during a storm event is nearly identical to the rate of change of the corresponding wind speed. For example, the modeled waves in storm *a* go from near 0 cm to above 30 cm and back to near 0 cm at the same rate that the wind goes from 1 m/s to greater than 8 m/s to less than 5 m/s. Similarly, the modeled wave heights in storm *b* go from approximately 10 cm to 20 cm at the same rate that the wind increases from approximately 5 m/s to 7 m/s. However, the observed waves do not follow this same relationship. In fact in all six storm events the observed wave heights increase from near 0 cm to a maximum very quickly, regardless of the rate of change of the wind speed.

Outside of the storm events, when the observed waves fall below approximately 10 cm, the model generally overestimates the wave heights (Figure 3.2). In some cases, such as DOY 284.6, the model overestimates by only a factor of two, but in other times, such as DOY 288.6 and 292.2, the model predicts waves when there are none observed. In both DOY 284.6 and 292.2 the wind speeds are approximately 2 m/s, but the wind direction is from the south and the east respectively. This difference in wind direction explains the smaller observed and modeled waves on DOY 292.2 compared to DOY 284.6, remembering that the fetch to the RBR pressure sensors is shortest during an easterly. However, it does not explain the overestimation by the model during an equivalent time step (see 3.4).

To assess the model performance during various events the mean significant wave height and model fit, expressed as the root mean square error (RMSE) and model skill (Willmott, 1982), are presented in Table 3.1. The model skill, also known as the index of agreement, yields a value of 1 when the observations and model results are in perfect agreement and a value of zero when they are in complete disagreement. It is worth noting that while the dimensionless skill values can be compared between events the RMSE values cannot. In five of the six storm events (a,c-f) the model skill was much greater than 0.5 indicating that the modeled and observed wave heights were generally in good agreement. Moreover, in storm event *a* the similarity of the observed and modeled mean significant wave height along with the high model skill and low RMSE value indicate an extremely accurate prediction. This is also seen, to a lesser extent, in storm events *d-f*. The low model skill and high RMSE value associated with events less than 10 cm further illustrates the models tendency to overestimate small amplitude waves.

While the significant wave height provides a rough idea of the statistical distribution of wave heights during a given window in time a more complete picture of the wind wave field is achieved with the wave spectrum. In Figure 3.3 the observed and modeled wave spectra, with energy spectral densities

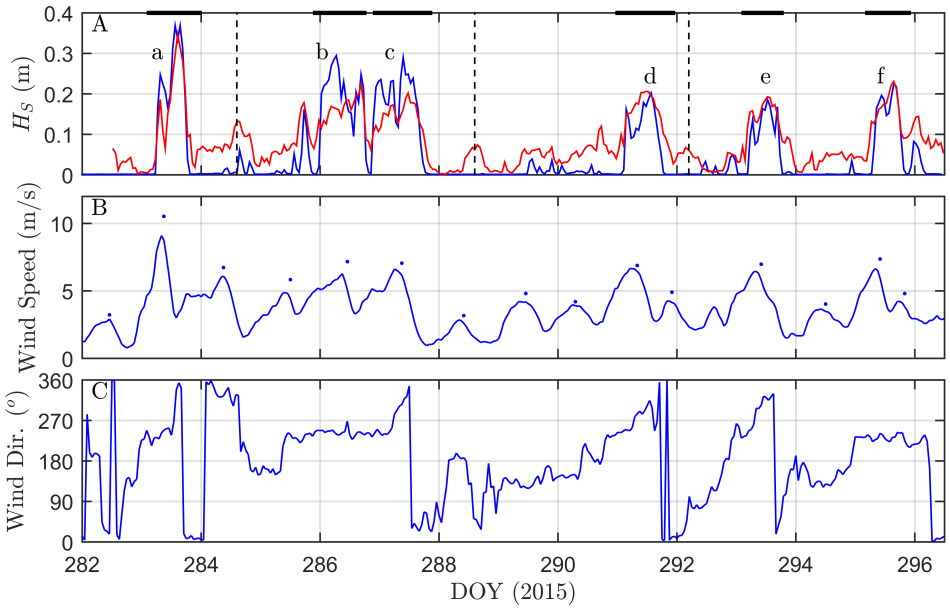

Figure 3.2: Simulated (—) and observed (—) significant wave heights (A) along with daily maximum wind speed (·), hourly average wind speed (B), and direction (C) during the 2015 sampling period. The length of each of the six storm events (a-f) is indicated by a thick black line at the top. The vertical dashed lines from left to right indicate DOY 284.6, 288.6, and 292.2 respectively

Table 3.1: Statistical comparison of the observed and modeled significant wave heights in 2015 during storm events and in calm periods.

	H_s Mean (m)			
Event	Field	Model	H_s RMSE (m)	H_s Skill
a	0.129	0.124	0.054	0.949
b	0.188	0.161	0.074	0.538
c	0.171	0.142	0.064	0.732
d	0.091	0.145	0.062	0.778
e	0.105	0.148	0.052	0.758
f	0.114	0.151	0.057	0.818
≤0.1 m	0.010	0.057	0.055	0.484

below 1.5×10^{-2} m^2/Hz removed, is presented. A high value of the energy spectral density represents large wave heights. Additionally, the distribution of energy indicates the wave periods present in an event with the maximum in energy corresponding to the wave field's dominant period. During the six storm events (a-f) the phase of the simulated spectra (Figure 3.3B) is inline with the observed spectra (Figure 3.3A) and for the most part the distribution of energy across periods is comparable. However, as the model overestimates small amplitude waves, the simulated wave spectra shows energy outside the storm events that is not present in the observed spectra. Additionally, events *b* and *c*, which showed the poorest match in Table 3.1, have much more variability in spectral energy in the observed spectra than the modeled spectra. Furthermore, the observed spectra in general indicates a larger range of wave periods present than the modeled spectra.

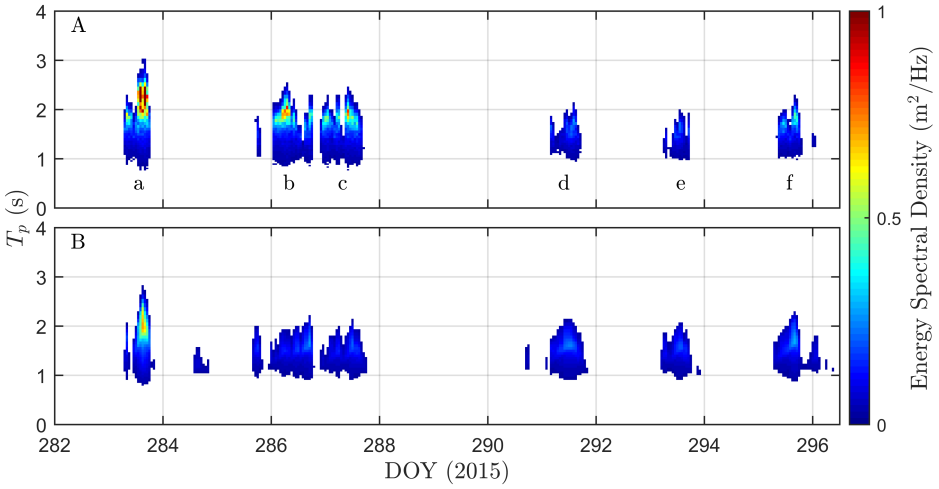

Figure 3.3: Comparison of the observed (A) and modeled (B) wave spectra during the 2015 sampling period. All spectral energy below 1.5×10^{-2} m^2/Hz has been filtered out. High spectral energy indicates larger wave heights than lower spectral energy. The dominant wave period during a given time interval is associated with the peak in the energy of the wave spectra.

3.3.2 Model Validation

The observed and modeled significant wave heights during a 24 day subset of the 2016 sampling period are shown in Figure 3.4A. Parallel to what

was observed in the 2015 model calibration the SWAN model overestimates small amplitude waves, but accurately predicts the magnitude and duration of storm events. Furthermore, the influence of the wind direction once again appears to play a large role in the agreement between the modeled and observed significant wave heights. Notice that when the fetch length is short, such as when the wind is from the southeast through northeast sector, the modeled waves vary the greatest from the observations. Additionally, as seen in the 2015 modeling results, the model skill decreases as the number of peaks in a storm event increases. For example, notice the near perfect fit of the storm event at DOY 261 compared to the storm event at DOY 277.

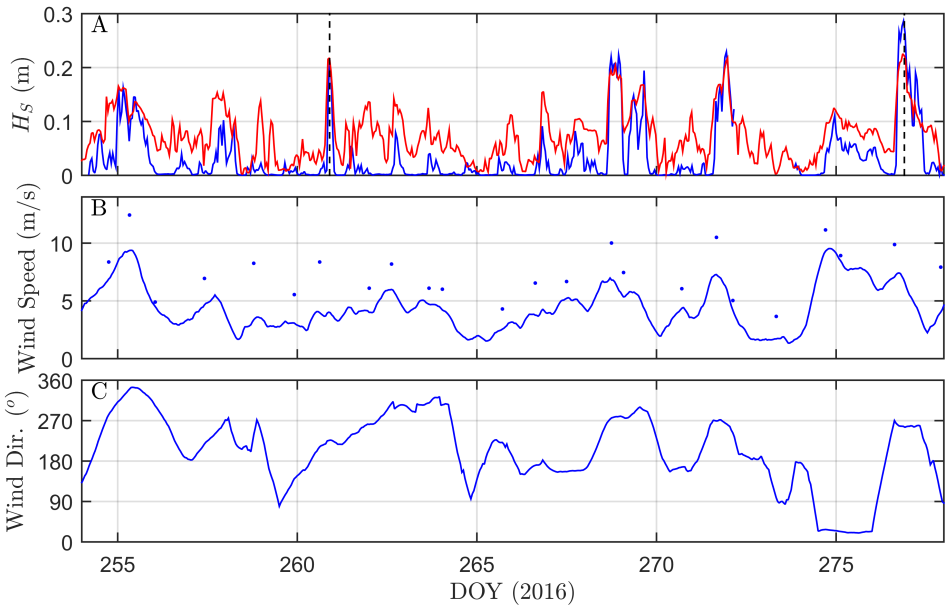

Figure 3.4: Simulated (—) and observed (—) significant wave heights (A) along with daily maximum wind speed (·), hourly average wind speed (B), and direction (C) during the 2016 sampling period. The vertical dashed lines indicated DOY 261 and 277, respectively.

To further address the models tendency to overestimate small amplitude waves a scatter plot of the observed versus modeled wave heights is shown in Figure 3.5. It is clear that when the observed waves are less than 10 cm the model overestimates wave heights, and the smaller the observed wave heights are the greater this overestimation is (Figure 3.5). Discussed in detail in section 3.4, this overestimation is likely a result of inaccurate wind

inputs, poor model resolution at high frequencies, or potentially the model not accounting for the dampening effect of hydrocarbons on high frequency wind waves. In contrast, when the observed waves are greater than 10 cm the model accuracy improves dramatically (Figure 3.5). This point is further enforced by the statistics presented in Table 3.2.

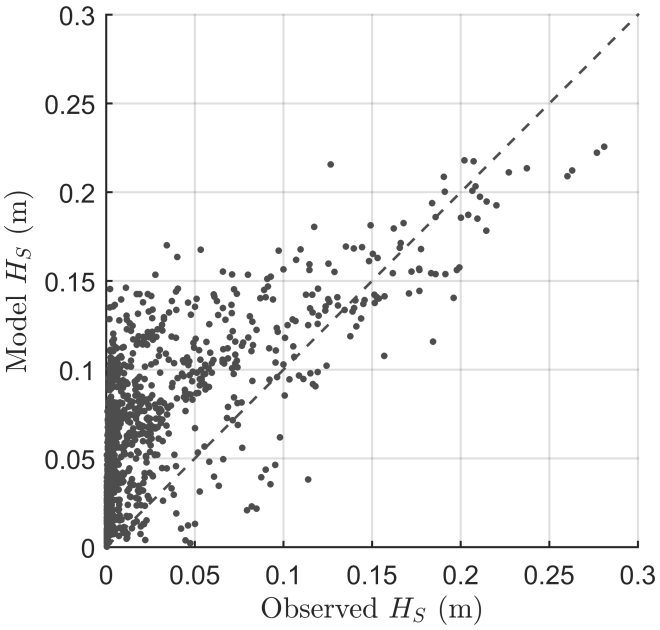

Figure 3.5: Observed versus modeled significant wave heights during the 2016 sampling period. The dashed line indicates a 1:1 ratio or perfect agreement of the model.

Table 3.2: Statistical comparison of the observed and modeled significant wave heights during the 2016 sampling period.

	H_s Mean (m)			
Event	Field	Model	H_s RMSE (m)	H_s Skill
All	0.026	0.063	0.040	0.731
≤0.1 m	0.014	0.058	0.054	0.479
>0.1 m	0.155	0.152	0.029	0.857

3.3.3 Resuspension

The linear wave theory expression for bottom orbital velocity, U_b, is given in Equation 3.1. Although this leads to an adequate estimation a more accurate representation of bottom orbital velocity is achieved by applying Equation 3.1 to the surface wave spectrum (Wiberg and Sherwood, 2008). This subsequently results in a spectral estimate of the bottom orbital velocity (Equation 3.2). From Equation 3.2 the significant bottom orbital velocity, U_{bs}, analogous to the significant wave height, can be found (Equation 3.3).

$$U_b = \frac{\pi H}{T \sinh(kd)} \tag{3.1}$$

$$U_b = \sqrt{2 \int_0^\infty \frac{4\pi^2}{T^2 \sinh^2(kd)} S_{\eta\eta} d\omega} \tag{3.2}$$

$$U_{bs} = \sqrt{2} U_b \tag{3.3}$$

A comparison of the modeled and observed significant bottom orbital velocities at the location of the RBR pressure sensors, approximately 3 meters deep, during the 2015 and 2016 sampling period are shown in Figure 3.6. To asses when resuspension occurred a laboratory determined critical bottom orbital velocity, U_{Cr}, of 5 cm/s for FFT is denoted (Lawrence et al., 1991). In 2015 spikes in the significant bottom orbital velocity were associated with the six storm events (a-f) (Figure 3.6A). However, in the observed orbital velocities only storm event *a* lead to resuspension and the model predicted orbital velocities never exceeded the critical threshold. Notice the underestimation of the modeled significant orbital velocities in events *b* and *c* and recall that the modeled significant wave heights during these events were also underestimated. The significant bottom orbital velocities during a 24 day subset of the 2016 sampling period were on average less than the 2015 period (Figure 3.6B). During this time the observed orbital velocities exceeded the resuspension threshold in one storm event and the modeled orbital velocities never exceeded 2 cm/s.

To gain an idea of the frequency of resuspension events that occur in BML an extreme value analysis was conducted. The observed significant bottom orbital velocities during the 2015 and 2016 sampling periods that were greater than 1.5 cm/s were recorded. Then, to assure statistical independence, only the largest of these recorded events every 6 hours was kept. This is roughly the time for a storm to pass. From this data set a Gumbel distribution was fit and the expected occurrence or return period, T_R, of a

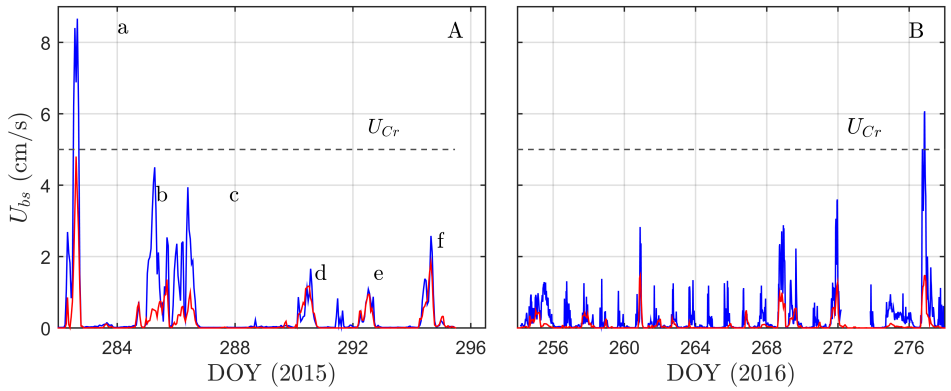

Figure 3.6: Simulated (—) and observed (—) significant bottom orbital velocities (U_{bs}) during the 2015 (A) and 2016 (B) sampling periods. The six storm events (a-f) in 2015 are indicated (B). The critical bottom orbital velocity (U_{Cr}) required for resuspension of FFT is denoted.

given value of U_{bs} could be extrapolated to future events. Figure 3.7 shows the return period of a given significant bottom orbital velocity. As expected, since the duration of the 2015 and 2016 sampling period combined was 68 days, the largest observed event in this time frame had an expected return period of 68 days. Additionally, the return period of a bottom orbital velocity equal to the resuspension threshold of 5 cm/s is approximately 23 days (Figure 3.7). The dashed line in Figure 3.7 represents the magnitude of the orbital velocities that are statistically possible given enough time. However, given the fetch limited nature of the waves a bottom orbital velocity greater than approximately 15 cm/s in 3 meters of water is highly improbable.

The modeled significant bottom orbital velocities on the coarse and nested BML SWAN domains for storm event *a* and the 10 year wind event (17 m/s) are shown in Figure 3.8. During storm event *a* the bottom orbital velocities in the littoral zone and along selected areas of the shoreline exceed the resuspension threshold (Figure 3.8A). A closer look at the nested domain shows that resuspension is concentrated to the immediate shoreline and that bottom orbital velocities are weak just offshore (Figure 3.8B). The 10 year wind event creates large wave heights which in turn leads to high bottom orbital velocities. In the littoral zone these velocities exceed 35 cm/s and much of the nearshore areas are above 10 cm/s (Figure 3.8C). Additionally, the nested domain shows that velocities directly onshore are upwards of 20 cm/s and that even offshore the velocities are still near the resuspen-

sion threshold. While the 10 year wind event could be considered rare, its occurrence would cause significant sediment resuspension and transport.

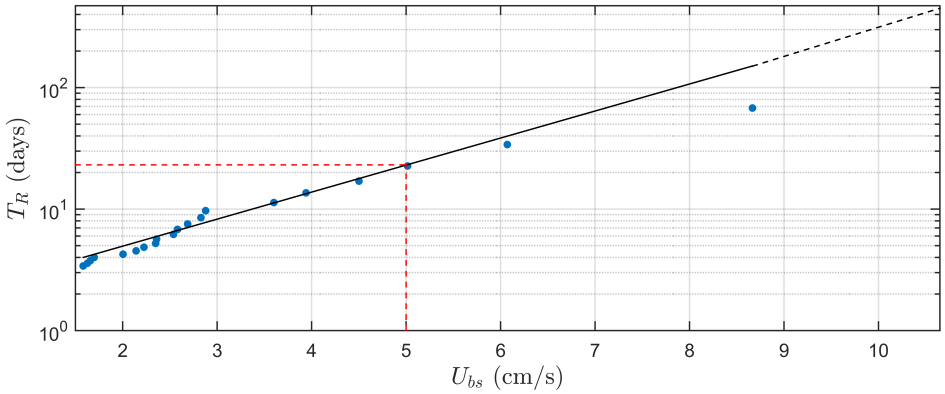

Figure 3.7: Estimates of the return periods for significant bottom orbital velocities. The observed data (·) is fit with a Gumbel distribution (—) and extrapolated to more remote occurrences of U_{bs} (−−).

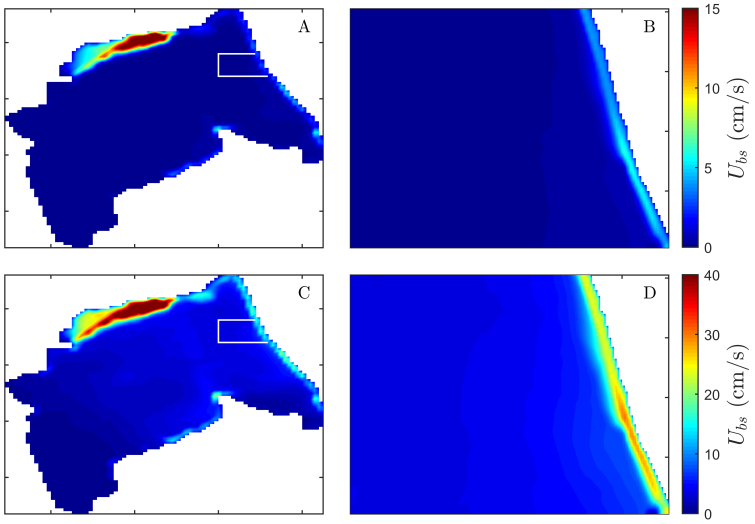

Figure 3.8: Significant bottom orbital velocities on the coarse and nested SWAN domains for storm event *a* (A,B) and the 10 year wind event (C,D).

3.4 Conclusions

The SWAN model was used to simulate the wave heights on BML during the 2015 and 2016 sampling periods. In both years the model accurately predicted the magnitude and duration of the storm events ($H_S > 10$ cm), but consistently overestimated wave heights during calm periods ($H_S \leq 10$ cm). It was found that the modeled wave heights during a storm event matched the observations best when the corresponding wind speed had a well-defined and sharp peak, and the direction had minimal variation and was out of the Southwest. Additionally, the failure of the model to simulate wave height variations within a storm event on the order of a few hours is potentially a result of the wind speed and direction sampling rate being too slow. In the future inter-hourly wind data would lead to better model agreement within storm and calm events alike.

The overestimation of small amplitude waves by SWAN has been documented in the literature and attributed to a number of factors (Seibt et al., 2013). In this study there are two factors that present themselves as likely culprits. The first is that since the wind is measured off-site it does not account for the effects of the surrounding lake topography on the wind speed and direction. For example, a wind from the East measured at the water surface next to the instruments would be greatly diminished by the adjacent lake embankment, while the off-site wind would have no knowledge of this reduction. Therefore, it is very probable that the when the wind direction is out of the southeast through northeast sector the wind speed, used to force the SWAN model, is an overestimation of the wind that generated the observed waves. A meteorological station positioned on the shore adjacent to the instruments or on the instrument post itself would likely lead to better agreement between the modeled and observed wave heights in calm periods. The second factor contributing to the overestimation is that the presence of hydrocarbons on BML has been shown to dampen high frequency wind waves (Chapter 4). As the model does not incorporate this dampening effect it could be that the model predicted wave heights during calm periods are what would actually be observed in the absence of hydrocarbons, hence the overestimation.

During the 2015 and 2016 sampling periods the observed waves rarely generated bottom orbital velocities capable of causing sediment resuspension at a depth of 3 m. Additionally, it was found that the return period for a resuspension event in 3 m of water was approximately 23 days. The SWAN model was used to estimate the significant bottom orbital velocities during two storm events at all depths within BML. It was found that during the 10

year wind event, when the fetch limited significant wave height approached 60 cm, the significant bottom orbital velocities caused resuspension in only the nearshore areas and at depths less than 4 m. Therefore, as BML is a former mine pit with steep sidewalls, there are few areas where the water depth is shallow enough for sediment resuspension, due to bottom orbital velocities, to occur.

Chapter 4

Effects of Hydrocarbons on Wind Waves

4.1 Introduction

A leading challenge in the oil sands industry is the storage and reclamation of bitumen extraction byproducts such as fluid fine tailings and oil sands process affected water. One potential reclamation strategy is to turn a mined out pit into an end pit lake by backfilling the pit with fluid fine tailings and capping it with oil sands process affected water (Lawrence et al., 2016). In 2013, Base Mine Lake (BML), became the first full scale demonstration end pit lake in the oil sands industry. One specific interest in BML is the presence of hydrocarbons, residual bitumen from the extraction process, on the lakes surface and their effect on wind waves. It has been observed that, in the presence of hydrocarbons, there is a reduction in surface ripples and a general damping of wind waves. Since wind waves can cause mixing in the water column, lead to sediment transport and erosion in the nearshore, and directly affect the fluxes of gas, momentum, and heat through the air-water interface, their modification is key in understanding the reclamation process. While a variety of laboratory studies have been conducted to examine the calming effect of oil on wind waves (Broecker, 1978; Liu and Lin, 1979), few field studies have been performed.

In this study we seek to examine the effect of oil on wind waves both in the laboratory and the field. First a brief history on the effect of oil on waves is given, then the generation of wind waves on clean and oil contaminated surfaces is described, followed by the laboratory and field methods. The results of the laboratory and field experiments are then reviewed, and the implications of a modified wind wave field on physical processes in BML are discussed.

4.2 Historical Background

Since ancient times people have been fascinated with the effects of oil on wind waves. Records from the 1st millennium AD describe ships pouring oil on rough seas in order to calm the waves, and over the next 800 years tales of the calming effect of oil on water appear sporadically (Fulford, 1968). Then Franklin et al. published "Of the Stilling of Waves by Means of Oil" which drew simple yet important conclusions formed over the course of numerous experiments, the most famous carried out at a pond in the Clapham district of South London (Franklin et al., 1774). Franklin, adding only a teaspoon of oil on the windward side of the pond, observed a patch of water, roughly an acre in size, become still as glass in a short period of time. From this and other experiments, Franklin concluded that oil prevents the formation of new waves, and reduces the presence of small waves and whitecaps within a swell, but does not affect the height of large waves.

During the next century the calming effect of oil on water attracted not only scientific but commercial interest. Politicians in Britain lobbied for ships to carry tanks of oil for discharge in rough weather, and the US Life-Saving Service (the precursor to the US Coast Guard) looked into the use of oil during rescues (Sparrow, 1883; Giles, 1969). On the scientific side, Aitken (1884) ascertained through laboratory experiments that it is a reduction in surface tension that leads to a diminished number of ripples. Then Pockels (1893) found that while the reduction of surface tension plays a role in wave damping it cannot be the entire cause. This work ultimately led Reynolds and Langmuir to postulate that gradients in surface tension are key in the damping effect of oil on wind waves (Reynolds, 1880; Giles, 1969).

4.3 Theoretical Background

When a wind blows above a critical speed over an undisturbed water surface small ripples known as capillary waves are the first to form (Kinsman, 1965). These waves have wavelengths less than 1 cm and surface tension is the dominant restoring force. As long as the wind continues to blow, and the energy input from the wind is greater than the rate of energy dissipation, the capillary waves will grow larger. Once the waves reach a length of 1 cm they begin to experience the restoring forces of gravity as well as surface tension. Eventually, when the wavelength exceeds 3 cm, the gravity effects dominate, and the waves continue to grow in both length and amplitude until there is a balance between energy input from the wind and energy dissipated.

At this point the wind wave field is fully developed and, while the largest waves cease to grow, new capillary waves form on the wave faces and start the process anew. This fully developed sea state consists of capillary, gravity-capillary, and gravity waves all with different wavelengths and traveling at different wave speeds. The wave speed, $c = \omega/k$, and wavelength, $\lambda = 2\pi/k$, where ω is wave angular frequency and k is wavenumber, are related according to the dispersion relation:

$$\omega^2 = \left(gk + \frac{\sigma k^3}{\rho} \right) \tanh(kd) \tag{4.1}$$

where g is local gravitational acceleration, ρ is fluid density, σ is surface tension, and d is fluid depth. In the case of deep-water waves ($d > 0.5\lambda$), the $tanh(kd)$ factor approaches one so that the deep-water wave speed, c_o, is given as:

$$c_o = \sqrt{\frac{g}{k} + \frac{\sigma k}{\rho}} \tag{4.2}$$

Using $d = 1$ m, $\rho = 1000$ kg/m^3 and $\sigma = 7.2 \times 10^{-2}$ N/m, the wavelength dependence of the wave speed is shown in Figure 4.1. For this case there is a minimum wave speed at a wavelength of 1.73 cm. From this minimum, gravity waves move faster with increasing wavelength, and capillary waves move faster with decreasing wavelength.

The presence of an oil film does not completely alter the mechanisms of wind wave generation, but does change the energy input and rate of amplitude dissipation. A reduction in surface tension associated with an oil film increases the critical wind speed needed for wind wave generation (Kawai, 1979). This means that it takes a faster wind to deform the now "smoother" surface and the oil film inhibits the flux of momentum at wind speeds below this critical value. Additionally, the presence of oil leads to an increased rate of energy dissipation in capillary waves due to a phenomenon known as the Gibbs-Marangoni effect (Lucassen-Reynders and Lucassen, 1970; Behroozi et al., 2007). This results in an enhanced attenuation of capillary waves and therefore a shift in the most unstable wavenumber to smaller wavenumbers. This shift means a developing wind wave field is dominated by waves with longer wavelengths and diminished growth rates (Creamer and Wright, 1992).

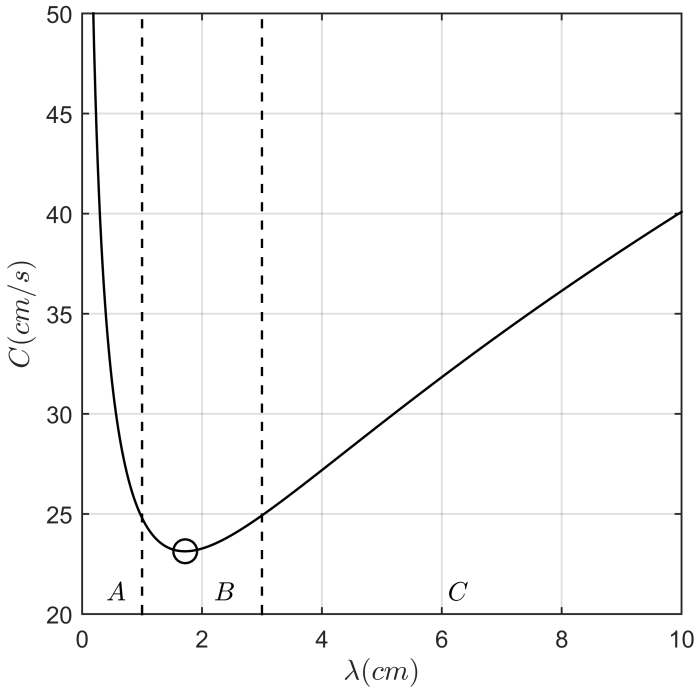

Figure 4.1: The complete dispersion relation for surface water waves. Regions A, B, and C refer to the capillary, gravity-capillary, and gravity wave regimes, respectively. The capillary wave regime is defined as surface tension contributing $> 75\%$ of the restoring force, and the gravity wave regime as surface tension contributing $< 25\%$ of the restoring force. The minimum phase speed (O) occurs at a wavelength of 1.73 cm

4.4 Experimental Method

4.4.1 Laboratory

Wind waves were generated in an open top rectangular Plexiglas tank (50 x 10 x 38 cm) attached at one end to a wind tunnel (50.5 x 10 x 15 cm) fitted with four flow straighteners (Figure 4.2). The fan produced wind velocities of approximately 6 m/s, and the long sides of the trough were raised so that a more uniform wind field could be generated across the water surface. As a result of the wind, a current moving down the tank at 3 cm/s was observed. The tank was filled with 19 L of tap water and dyed with rhodamine. A small inflow of water, used to give a continuous overflow, reduced wave reflections

and prevented the buildup of oil at the downwind end of the tank.

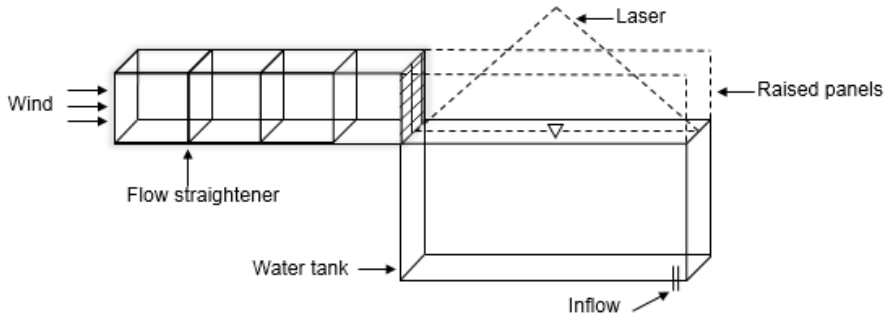

Figure 4.2: Diagram of the laboratory setup

A green laser was mounted above the tank to illuminate the water surface and wave characteristics were measured in the dark by recording the vertical oscillation of the laser light sheet with a Panasonic GH4 camera running at 90 fps mounted in front of the tank. The pixel location of the recorded interface was found by identifying the center of mass of light intensity of each column of pixels (1920 columns). Any remaining noise from the extracted interface was removed with filtering techniques.

To observe the effect of oil on the wind waves, an oil film was created by injecting extra virgin olive oil (Triolein) from a syringe onto the waters surface at the upwind end of the tank. This was done after achieving a fully developed wind wave field on a clean water surface. Approximately 5 cm^3 of oil was injected over 10 s, and dispersed by the wind across the water surface.

4.4.2 Field

To compare wind wave generation in BML in the presence and absence of oil, a section of the water surface was isolated from hydrocarbons. A rectangular oil boom (4.5 x 6 m), anchored in 4 locations, was deployed around a fixed instrument post. The boom arms were constructed with commercially available foam rods, 7 cm in diameter, and fitted with a weighted plastic skirt that hung 45 cm into the water. During a period when the water surface was relatively hydrocarbon free, the boom was deployed and left for three weeks. The fetch inside the boom was large enough so that capillary and gravity-capillary waves, both affected by oil, could be generated by the

wind. Shortwaves generated outside the boom were blocked by the boom arms, but longer waves were able to propagate inside.

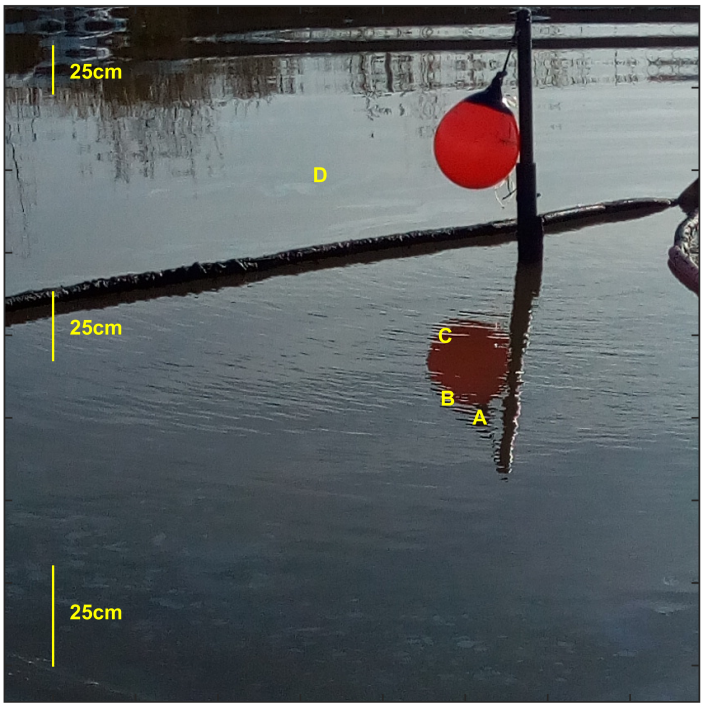

Figure 4.3: Digital image of the oil boom with analyzed points in the boom (A-C) and outside the boom (D). The wind is from the top right to bottom left and tree reflections are present in the top of the image

At intermittent periods throughout the boom deployment, images of the water inside and outside the boom were captured with an 8 megapixel digital camera. Since wave crests and troughs appear as different image light intensities, due to differences in light reflection, the wavelengths could be determined. It was found that analyzing the waves inside the boom near the edge of the reflection of a red mooring buoy gave the best contrast and provided more confidence as to the location of the crests and troughs (Figure 4.3). Additionally, in the images, the pixel resolution goes from fine to coarse moving away from the foreground. To correct for this distortion, objects of known length in the foreground and background were chosen and their pixel to length ratio were determined. A pixel to length ratio for each row and column was then assigned through linear interpolation. Each

location of the analyzed wave field was chosen far enough away from the boom and instrument station so that wave interference was minimized. The wind speed and direction during the boom deployment were recorded and the amount of oil present inside and outside the boom was visually noted in the images.

4.5 Results

4.5.1 Laboratory

Visualization of the effect of oil on wind waves generated in the wave flume is shown in a time-space plot (Figure 4.4a). This figure represents a compilation of interface heights observed in 2500 images collected over 28 s (only the middle 13 s are shown). During the experiment the wave field underwent four obvious changes in wave characteristics indicated by regions A-D. Initially, before the fan was turned on, the water surface was free of oil and waves (A). Then, after the fan was started, a developing wind wave field - a wave field that is not yet fetch limited - was observed (B). Since the wind did not impact the water surface for the first 5 cm, and wave reflections were present in the last 5 cm, results in these regions were ignored. In a short time the developing wind wave field transitioned into a fully developed wind wave field and waves propagated with fairly uniform wave speed, wavelength, and amplitude (C). Lastly oil was applied to the water surface and immediately the amplitude of the waves decreased at the windward end of the tank (D). After a few seconds, the oil was spread across the tank and the entire wind wave field was damped out.

To better understand the change in wave amplitude during the experiment, a time transect at the center of the tank is shown (Figure 4.4b). Notice the growth of the developing wind waves (A), and that the fully developed wind wave field (C) contains wave packets, a consequence of the dispersion relation. Upon the addition of oil the wave amplitudes resemble those in the early stages of a developing wind wave field (D). This is illustrated by the immediate reduction in amplitude from ± 0.15 cm in (C) to ± 0.03 cm in (D).

To gain further insight into the physical mechanisms at work, 2D wave spectra were computed using the Fast Fourier transform (FFT) function in MATLAB. Comparing Figure 4.5a for the clean surface to Figure 4.5b with an oil film, it is clear that the oil film dampens high frequency waves. This is shown as a reduction in spectral energy above 10 Hz and elimination above 20 Hz. In addition, noting that wave energy is proportional to wave ampli-

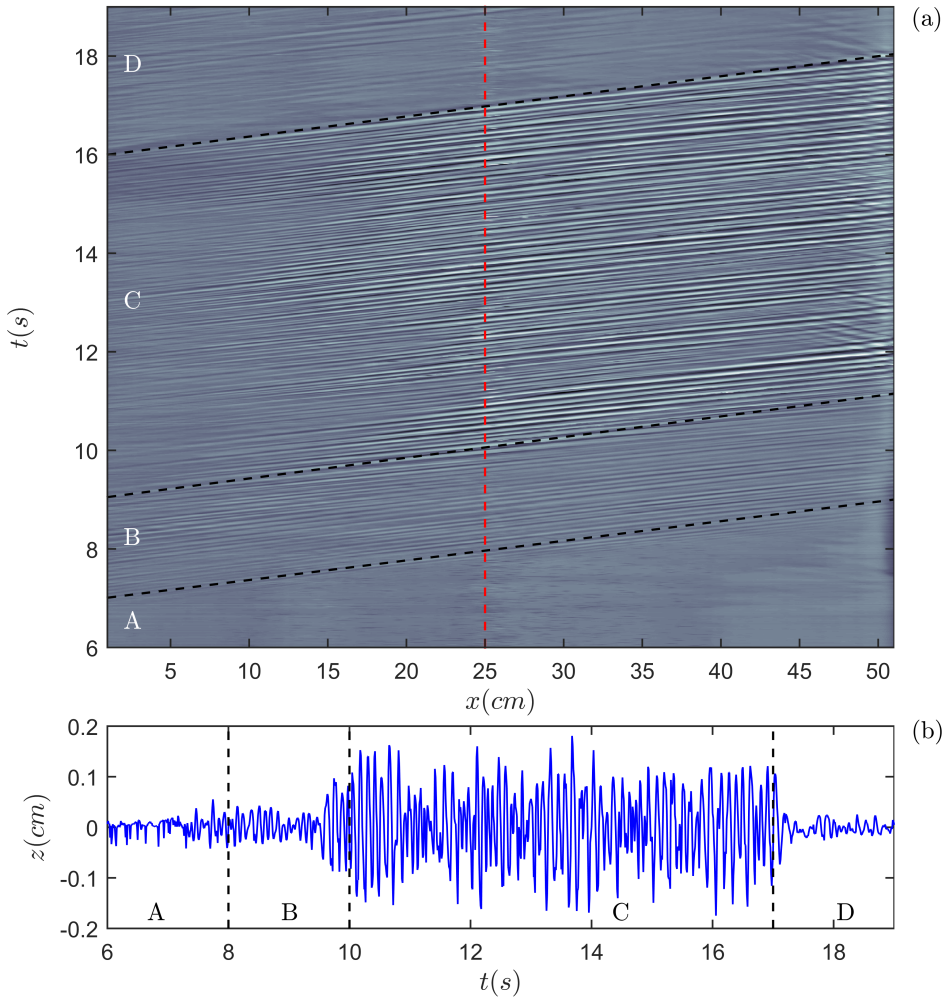

Figure 4.4: a) Plot of the deviation of the surface elevation from along the tank with increasing time. The wave characteristics for the (A) calm surface, (B) developing wind wave field, (C) fully developed wind wave field, and (D) wind wave field in the presence of olive oil applied at $x = 0$ cm and $t = 16$ s, are shown. Shading represents the wave amplitude with white indicating a crest and black indicating a trough. b) Wave amplitude with time at $x = 25$ cm (−−) (A-D, Figure 4.4a)

tude squared, the oil has the effect of diminishing wave amplitudes at all wave numbers. In both Figures 4.5a and 4.5b the theoretical dispersion rela-

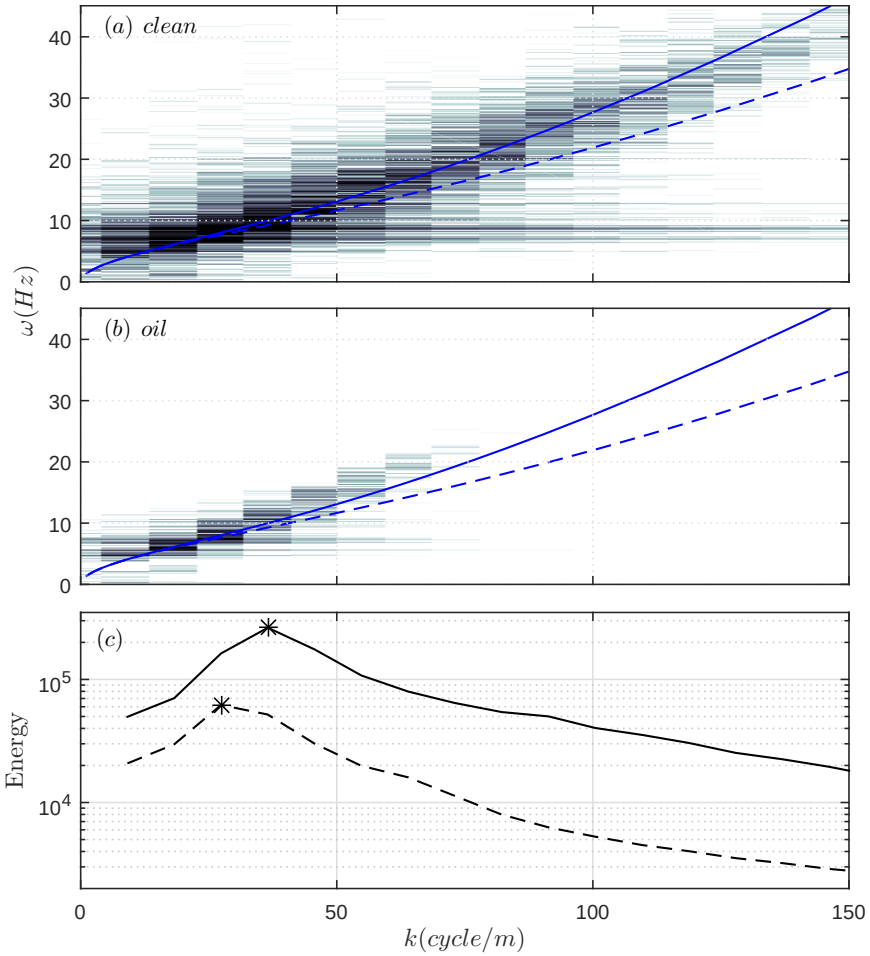

Figure 4.5: Spectral analysis of the laboratory generated waves on (a) the clean surface (25-40 cm and 11-15 s from region C, Figure 4.4) and (b) the oil contaminated surface (25-40 cm and 19-23 s from region D, Figure 4.4). Dark colors denote high energy. The dispersion relations (Equation 4.1) using the surface tension of water (-) and olive oil (−−) are overlaid. In (C) the energy at each wavenumber for water (−) and oil (–) surfaces along with the peak of the spectrum (*) are shown

tions on a clean and oil contaminated surface with a 3 cm/s wind generated flow are shown. The spectral energy in the absence of oil falls remarkably close to the theoretical dispersion relation for a clean water surface (Figure 4.5a). However, the spectral energy in the presence of oil also seems to fall

closer to the theoretical dispersion relation for a clean water surface than for a contaminated water surface (Figure 4.5b). This may be because the spectral energy in the presence of oil is associated with lower frequency waves which are less affected by an oil surface.

At each wavenumber in Figure 4.5a and 4.5b the energy was summed over ω and plotted in Figure 4.5c. The total energy as a function of wavenumber is plotted in Figure 4.5c. It is clear that all wavenumbers are much less energetic in the presence of an oil film. It is also apparent that the peak in the spectrum is shifted from 36 cm^{-1} (λ = 2.8 cm) on a clean water surface to 27 cm^{-1} (λ = 3.7 cm) on oil contaminated surface. This shift is statistically significant at the 95% confidence level and is qualitatively similar to the shift shown in the linear instability analysis of Creamer and Wright (Creamer and Wright, 1992). It is somewhat strange that the energy in the longest waves is not the same regardless of the surface contamination since oil has little effect on long waves. However, as the waves generated in the experiment never exceeded a wavelength of 6 cm it is not surprising that even the longest waves were still slightly affected by the oil film. If the experiment were extended to smaller wavenumbers (longer wavelengths) it is likely that these energies would become equal.

4.5.2 Field

The wind wave characteristics at three locations inside the boom (A-C) and one location outside the boom (D) were captured (Figure 4.3). Qualitatively there were more small ripples inside the boom (A-C) than there were outside (D). The wind at this time was blowing from the background to the foreground of the image and so the waves seen at A-C were also propagating in this direction. At the downwind end of the boom, the image foreground, there was an oil film inside the boom, but not present at A-D (Figure 4.3). This film can also be seen at location D. Looking at a plot of A-D showing normalized light intensity, it is clear that there are waves inside the boom, but none outside (Figure 4.6). This result matches our visual interpretation of Figure 4.3, and indicates a dampening of the wave field in the presence of an oil film.

To get an idea of the wavelengths present at (A-D) transects in y of each plot in Figure 4.6 are shown in Figure 4.7. Inside the boom the waves exhibit wavelengths ranging from 1.0-1.4 cm (Figure 4.7a-c) which falls to the left of the minimum in the dispersion relation, indicating that the waves are governed primarily by surface tension. Outside the boom there are no discernible waves and the fluctuations are likely noise (Figure 4.7d).

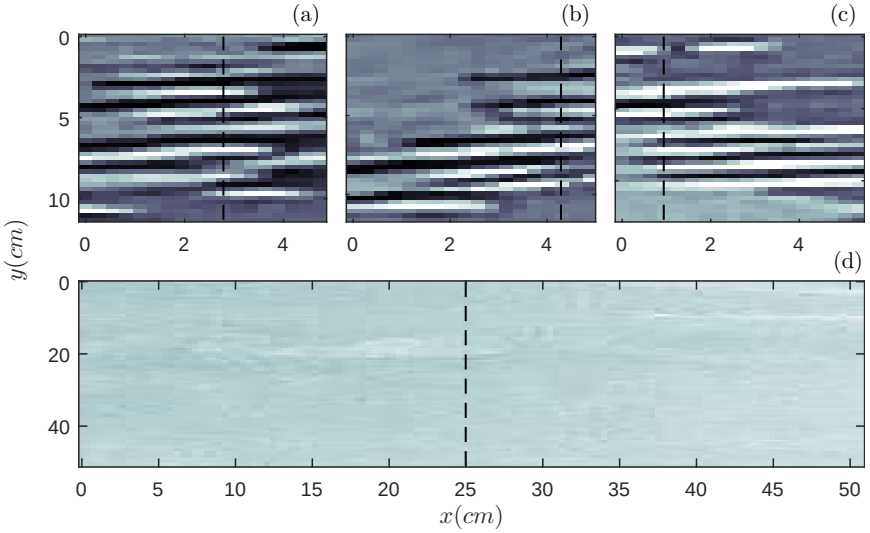

Figure 4.6: Plot of light intensity in regions A-D of Figure 4.3. Dark colors represent wave crests and light colors wave troughs. Transects in y (−−) are shown in Figure 4.7

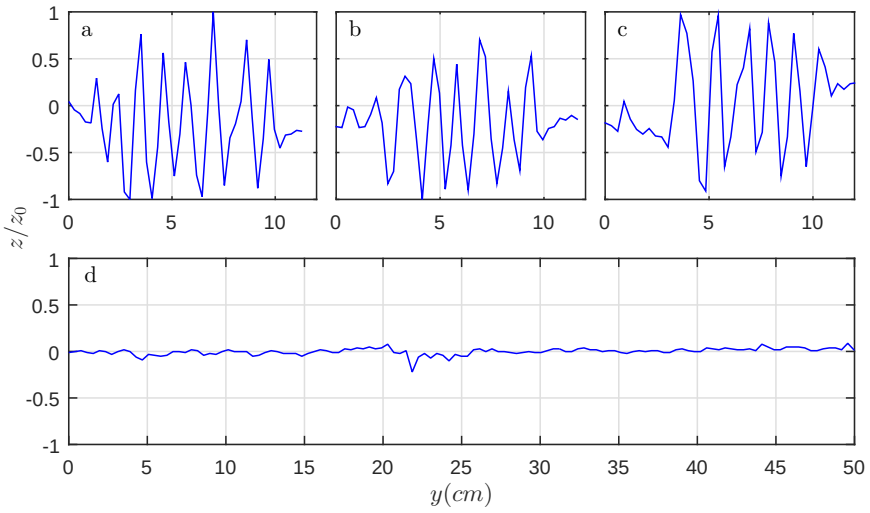

Figure 4.7: Wavelength transects for Figure 4.6 inside (A,B,C) and outside (D) the oil boom. Amplitude has been normalized by the maximum amplitude (z_o) of transect (a)

4.6 Conclusions

The results of laboratory and field experiments reveal a dramatic change in the observed wind wave field in the presence of an oil film. In both cases it is likely that the oil film is acting to dampen the flux of momentum through the air-water interface, thereby increasing the critical wind speed needed for wind wave generation as described by theory (Kawai, 1979). This means that to develop a similar wind wave field in BML, as found on a non-contaminated surface, a higher wind speed would be required. The observed dampening of capillary waves suggests that the net flux of momentum across the air-water interface in BML is less than it would otherwise be without an oil film. In the laboratory it was found that the addition of oil onto an already fully developed wind wave field dampened the waves and cause caused a shift in the peak wavenumber to smaller wavenumbers or longer wavelengths.

In summary, an oil contaminated surface leads to a wind wave field dominated by longer wavelength waves that take more time to develop and grow at a slower rate. Since wind waves are direct drivers of the physical processes in a water body it is postulated that the oil film on BML has not only decreased the flux of momentum from the wind, but likely affected lake circulation and the fluxes of gas and heat.

Chapter 5

Modeling Internal Waves

5.1 Introduction

A large collection of literature exists regarding basin scale internal waves or seiches. However, a vast majority of this work has focused on internal waves in the open and coastal ocean, bays and fjords, large lakes, and laboratory environments (Mowbray and Rarity, 1967; Stigebrandt, 1976; Beletsky et al., 1997; Liu et al., 1998). Only a handful of studies have examined internal waves in small and medium sized lakes, such as BML (LaZerte, 1980; Hodges et al., 2000; Pannard et al., 2011). In lakes of this size, where inflows and outflows are often minimal, basin scale internal waves are in large part responsible for subsurface motions (Hodges et al., 2000). These motions impact the fluxes of gas, heat, and nutrients throughout the water column and potentially lead to the formation of a turbulent benthic boundary layer (Hodges et al., 2000; Pannard et al., 2011). This turbulent layer can subsequently enhance mixing and sediment resuspension in the hypolimnion (Hodges et al., 2000; Pannard et al., 2011). Therefore, in order to parameterize mixing in a stratified system the internal waves must be correctly measured and modeled.

The application of 3D numerical models to stratified flows did not become practical until the development of turbulence closure schemes in the late 1970's (Mellor and Yamada, 1974, 1982). However, these turbulence closure schemes, such as the level 2.5 model of Mellor and Yamada (1982), have in large part been applied to oceanic circulation models. Additionally, it has been shown that in many cases the classical closure schemes underpredict the depth of the surface mixed layer brought on by wind forcing (Martin, 1985). In small and medium sized lakes, where the mixed layer depth directly determines the magnitude of the thermocline setup due to the wind, a wrongful estimation of the surface mixed layer ultimately results in an incorrect prediction of the internal wave amplitudes (Hodges et al., 2000). More recently however, the development of 3D numerical models that more accurately determine the mixed layer depth, aptly known as mixed layer models, have led to increased accuracy in the simulation of internal waves

(Hodges et al., 2000). Currently there are a number of 3D mixed layer models available to simulate internal waves in lakes. Although, only two, the Estuary and Lake Computer Model (ELCOM) and Delft3D Flow, have been used with some consistency. In both cases the models have been shown to give similar results in terms of the internal wave amplitudes and periods (Dissanayake et al., 2016).

Delft3D Flow (WL–Delft Hydrualics), developed for coastal, river, and estuarine areas, is a multi-dimensional (2D and 3D) hydrodynamic model (Delft Hydraulics, 2006). It calculates non-steady flow in a system resulting from tidal and meteorological forcing on a variety of horizontal and vertical grids. It can be performed in hydrostatic or non-hydrostatic mode, prescribed multiple turbulence closure models, and account for the effects of the earth's rotation on flow. It has been used to model storm surges and tsunamis, thermal stratification in lakes, and wave-driven currents among other things. Additionally, modules for computing sediment transport, water quality, biological activity, and surface wave formation have been successfully coupled to Delft3D Flow.

In this chapter the internal waves in BML are simulated in Delft3D Flow and compared to internal wave observations from platform 1, 2, and the D26 mooring during the 2016 sampling period. First the model setup is described and the choice of parameterization for the wind drag coefficient discussed. Then the results of the simulations are presented. Next, the effect of rotation on the internal waves in BML is examined. Lastly, the findings are summarized and the implications of the internal waves on the physical processes in BML is given.

5.2 Model Setup

Delft3D Flow was applied to BML during a four day period from July 10-14 2016. The flow was simulated on a horizontal rectilinear grid with a resolution of 50 $\times$ 50 m covering the extent of BML (Figure 3.1). A vertical grid was prescribed using the Z-layer model with 20 layers of resolution varying between approximately 100 cm and 25 cm (Figure 5.1). The resolution was finest around the thermocline, free surface, and bed in order to more accurately resolve the internal wave amplitudes and shear stresses. Model bathymetry was interpolated from single beam sonar data with 2 m resolution to the horizontal grid. The breakwater implemented in SWAN was removed from the flow model for simplicity (see section 3.2).

A vertically varying temperature profile taken from platform 3 (P3),

and applied uniformly in the horizontal, was used to initialize the model. The model was run with a time step of 30 s and forced with wind speed and direction recorded at Sandhill Fen Site 3. A k-ϵ turbulence closure scheme with a background horizontal eddy viscosity and diffusivity of 0.01 m^2/s and a background vertical eddy viscosity and diffusivity of zero was used. It was assumed that the effects of heat flux and surface waves on the mixed layer depth was negligible. This was deemed reasonable given the short simulation period and small amplitude of the wind waves. The model output of temperature, a proxy for internal waves, and horizontal velocity was recorded at platform 2, 3, and the D26 mooring every 2 minutes and for the entire domain every 5 minutes. A complete list of the model parameters is found in Table B.2.

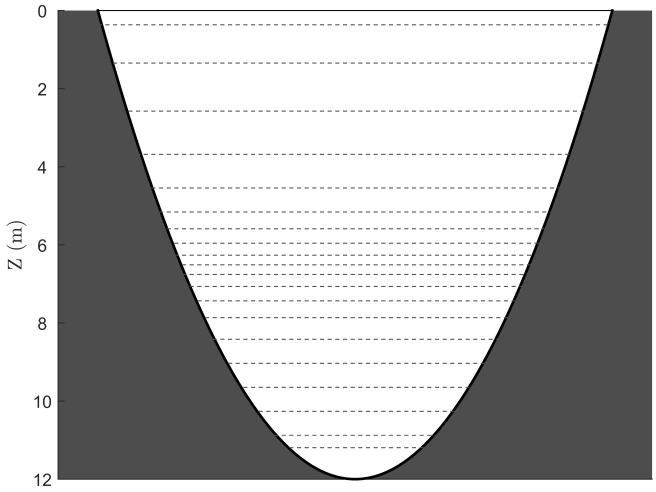

Figure 5.1: Idealized discretization of the vertical flow grid.

5.2.1 Wind Drag Coefficient

Within Delft3D Flow a non-uniform wind drag coefficient (C_d) can be prescribed based on wind speed. However, choosing wind drag coefficient values that are dissimilar to the empirical values of the system can result in over or underprediction of the mixed layer depth. Therefore, the wind drag coefficient values at various wind speeds on BML were calculated using measurements of the wind speed (U) and the momentum flux across the air-water interface (U^*) (Equation 5.1).

$$C_d = \frac{U^{*2}}{U^2} \tag{5.1}$$

$$U^* = \sqrt{\frac{\tau}{\rho_a}} \tag{5.2}$$

Where τ is wind stress and ρ_a is density of air.

Additionally, the observed wind drag coefficient values for BML were compared to values from the literature for small and medium sized lakes (Figure 5.2). It can be seen in Figure 5.2 that the wind drag coefficient at different wind speeds is generally in good agreement with the literature. The disagreement at higher wind speeds is most likely due to the rarity of those events on BML. The model wind drag coefficients were chosen to closely follow the observed coefficients while obeying the constraints of Delft3D Flow that no more than 3 slope values can be used (Figure 5.2).

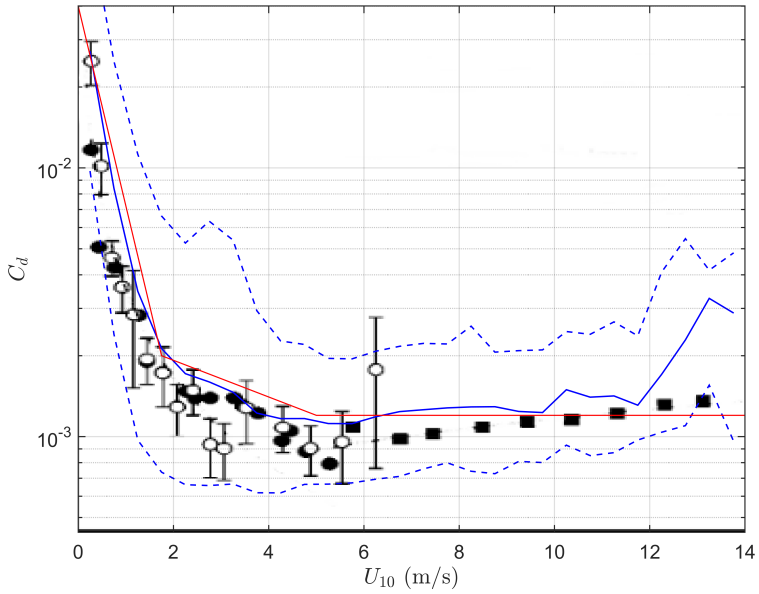

Figure 5.2: Observed wind drag coefficient (—) for BML compared to literature reported values for small lakes indicated by the circles and squares (Wüest and Lorke, 2003). The parameterized value of C_d used in Delft3D Flow (—).

5.3 Results

Since internal seiches are simply waves propagating along a density interface, specifically the thermocline, their amplitude is equal to the amplitude of the oscillations of the thermocline. Therefore, isotherms are used to depict internal wave height and period. A comparison of the observed and simulated isotherms in BML is shown in Figure 5.3. During this period the thermocline oscillates between approximately 3 m and 6 m with platform 2 exhibiting the largest internal wave amplitudes (Figure 5.3). In general, the periodicity of the simulated internal waves matches that of the observed internal waves (Figure 5.3). The simulated internal wave amplitudes are in good agreement with the observed amplitudes at platform 3 and D26 mooring, but underestimate the amplitude of the wave crests at platform 2 (Figure 5.3). Additionally, at platform 3 and D26 the gradient in the thermocline present during a wave crest and trough is on average larger than the gradient predicted in the simulations (Figure 5.3B,C). This is largely a result of too much mixing in the model which leads to discrepancies in the mixed layer depth. Notice the apparent increase in surface mixing or deepening of the mixed layer in the simulation at platform 2 (Figure 5.3D).

Table 5.1: Statistical comparison of the observed and modeled isotherms in 2016 using root mean square error (RMSE) and the model skill score of Willmott (1982).

Location	Isotherm	RMSE (^{o}C)	Skill
P2	15	0.68	0.71
	17	0.87	0.65
	19	1.08	0.72
P3	15	0.60	0.75
	17	0.65	0.78
	19	1.44	0.59
D26	15	0.55	0.82
	17	0.63	0.81
	19	0.84	0.75

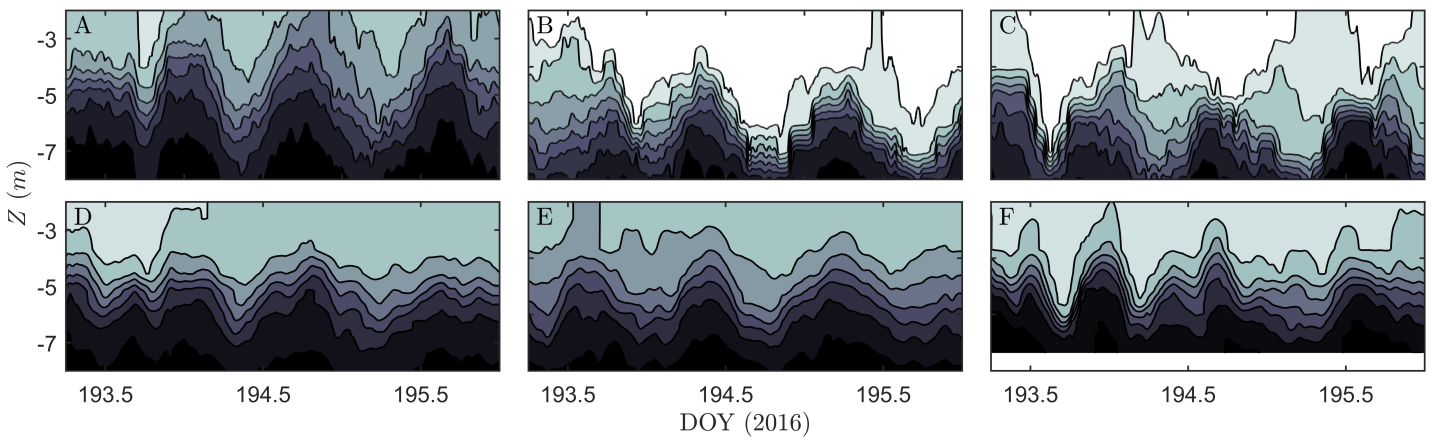

Figure 5.3: Observed (A-C) and simulated (D-F) isotherms for platform 2 (A,D), platform 3 (B,E), and D26 mooring (C,F). The contour closest to the surface is 21 ^{o}C and the contour interval is 1 ^{o}C.

To more systematically assess the model performance the root mean square error (RMSE) and model skill score of Willmott (1982) are computed. The skill score or "index of agreement" takes on a value of 1 when there is perfect agreement between the model and observed data and less than 1 when there is disagreement. From the statistics it is evident that the simulations perform best at D26 and poorest at platform 2 (Table 5.1). In addition, the model performs well at platform 3 in deep water but begins to deviate from the observations near the surface (Table 5.1). This deviation is also seen in Figure 5.3B,E.

A closer examination of the simulated and observed thermocline is achieved by analyzing an isotherm near the thermoclines center, in this case the 17 ^{o}C isotherm is chosen (Figure 5.4). At all stations the observed internal waves achieve a maximum wave height greater than 2 m and at platform 2 the waves exceed 3 m. The amplitude and period of the simulated internal waves at platform 3 and D26 are nearly identical to the observed internal waves (Figure 5.4B,C). At platform 2 the simulated internal waves are in phase with the observed waves and match the amplitude of the wave troughs, but underestimate the wave crests (Figure 5.4A). In all 3 locations the deviation of the simulated waves from the observed waves increases in time. This is likely attributable to a buildup of numerical error that results from poor estimates of mixing and a lack of modeled heat flux.

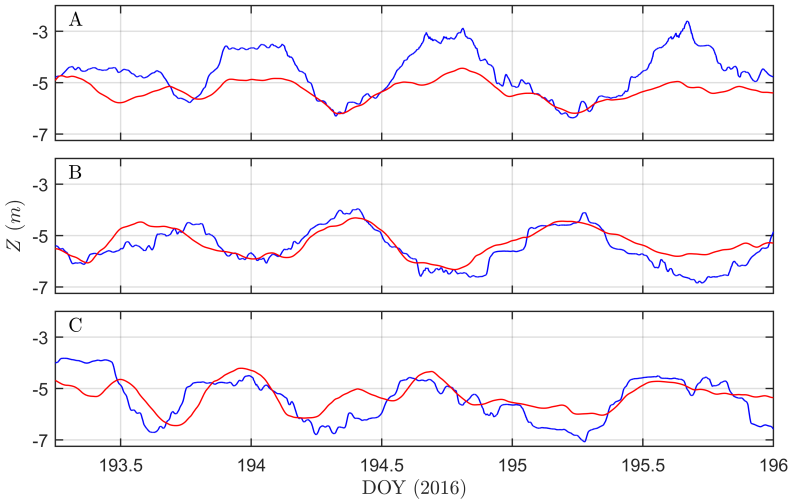

Figure 5.4: Simulated (—) and observed (—) 17 ^{o}C isotherm at platform 2 (A) platform 3 (B) and D26 mooring (C)

5.3.1 Rotational Effects

The effect of the earth's rotation on flow becomes important when the Rossby radius of deformation (L_R), a ratio of the wave speed to the Coriolis parameter, is of order or smaller than the length scale of the lake (Equation 5.3). In small and medium sized lakes surface gravity waves propagate to quickly to be affected by the earth's rotation. However, since internal waves propagate much slower, a consequence of a reduced gravity, their Rossby radius of deformation is much smaller.

$$L_R = \frac{\sqrt{g'd}}{f} \tag{5.3}$$

$$f = 2\Omega sin\theta \tag{5.4}$$

Where g' is reduced gravity, d is fluid depth, f is Coriolis parameter, Ω is earth's rotation rate, and θ is latitude.

In BML the Rossby radius of deformation is approximately 2.5 km, on the same order as the long fetch distance of the lake. Therefore, the basin scale internal waves may take the form of rotationally modified gravity waves such as Kelvin and Poincaré waves. The oscillatory motions of Poincaré waves are often indistinguishable from those of a linear seiche. And differ only in that the horizontal velocities associated with Poincaré waves rotate clockwise with time. Kelvin waves, on the other hand, are boundary trapped waves that rotate counterclockwise in the northern hemisphere and have a wave crest that is located along the boundary and decays exponentially towards the center of the basin.

Figure 5.5 shows the simulated internal waves and associated horizontal velocities at a depth 5 m in BML during the period July 10 20:00 to July 11 08:00 2016. Initially there is a strong impulse of wind out of the southwest that leads to a setup of the thermocline, upwelling and downwelling of water in the southwest and northeast corners respectively, and creates horizontal velocities indicative of a linear seiche (Figure 5.5A). Once the wind relaxes the thermocline begins to oscillate back towards equilibrium in the form of Poincaré and Kelvin waves. Examining Figure 5.5B-E the internal wave trough, indicated by the cold water, appears to hug the lake boundary and rotate in a counterclockwise direction through time. This is a Kelvin wave. While the internal wave crest also rotates in a counter clockwise direction, indicating a Kelvin wave, it's amplitude decays faster making it harder to discern (Figure 5.5B-E). Additionally, the horizontal velocities rotate clockwise in time and suggest that the basin scale seiche is in the form of Poincaré

waves (Figure 5.5B-E).

In order to better understand the effect of rotation on the internal waves in BML, simulations with and without the influence of the Coriolis force were performed. Figure 5.6 shows the maximum temperature difference that occurred between the two simulations at a depth of 5 m during the period July 10 to July 14 2016. Ignoring the Coriolis force produces large temperature differences, in some cases 5^oC, along the boundaries of BML (Figure 5.6). This is inline with the fact that Kelvin waves, present only with the influence of rotation, decay towards the basins center. Therefore, temperature deviations are smaller in the deeper areas of BML where the

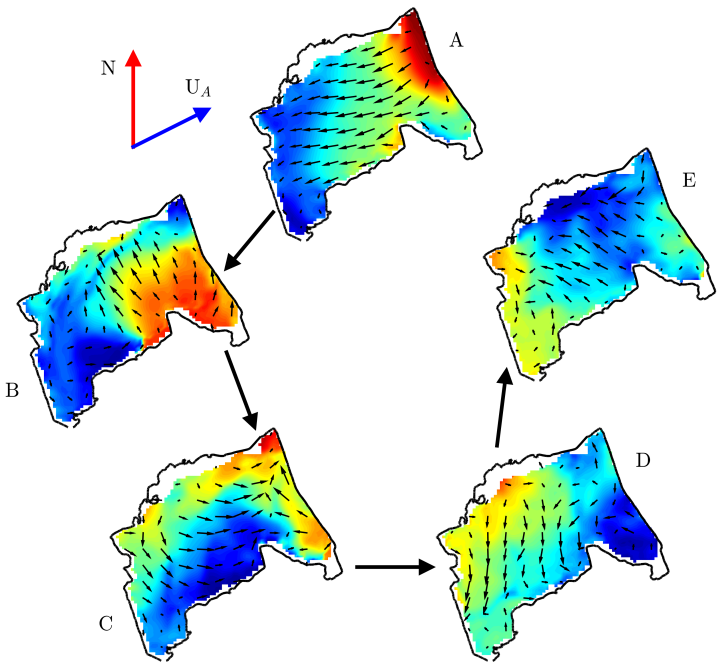

Figure 5.5: Simulated internal waves and horizontal velocities at a depth of 5 m in BML during the period July 10 20:00 to July 11 08:00 2016. The time starts at 0 hours (A) and steps forward in 3 hour increments (B-E). An impulse of wind (U_A) at time 0 leads to a setup of the thermocline (A). Once the wind relaxes a Kelvin wave, most easily visualized as the cold (blue) water, begins rotating counterclockwise around the basin (B-E). Additionally, the horizontal velocities rotate clockwise through time indicating a basin scale seiche in the form of Poincaré waves.

instrument moorings are located (Figure 5.6).

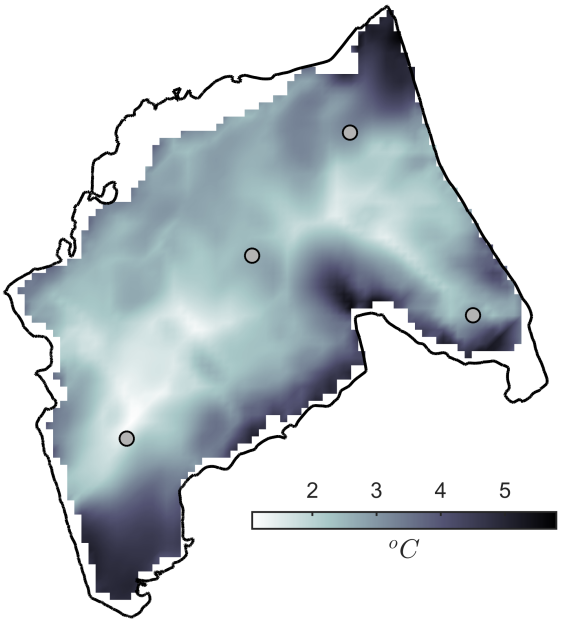

Figure 5.6: Effects of rotation on the simulated internal waves at a depth of 5 m in BML during the period July 10 to July 14 2016. The maximum difference in temperature between the simulations with and without Coriolis force is expressed in the heat map. The location of the three platforms (P1,P2,P3) and the D26 mooring are shown as grey circles.

5.4 Conclusions

Delft3D Flow was used to simulate the internal waves in BML during a four day period from July 10 to July 14 2016. A comparison of the observed and simulated isotherms throughout the water column at three locations (P2, P3, D26) showed that the model accurately predicted the periodicity and in most cases the amplitude of the internal waves. At platform 2 the magnitude of the observed wave crests along the 17 ^{o}C isotherm was significantly larger than the corresponding wave troughs. In other words the internal waves at platform 2 were less sinusoidal than the waves at platform 3 and D26. This resulted in the model underestimating the internal wave amplitude at platform 2.

The model estimates of the internal wave amplitudes became less accurate with time at all locations. This is likely a result of the simulated mixed layer depth becoming less accurate at each time step and therefore introducing numerical error into the following time step. It is plausible that if heat flux was incorporated into the model the buildup of numerical error with time would be reduced. Additionally, empirically determined values of the background horizontal and vertical eddy diffusivity and viscosity would likely lead to better estimates of the thermocline thickness and location as well as the surface mixed layer depth.

Typically 3D circulation models use a uniform value for the wind drag. However, it was shown that using a single value to define the wind drag coefficient is not an accurate parameterization and could result in inaccurate estimates of the surface mixing. Instead, the wind drag coefficient should be varied with wind speed and made to match either some observed values or a general function. In the case of BML the observed wind drag values were highest at low wind speeds, decreased to a minimum at approximately 5 m/s, and increased again at higher wind speeds.

Since BML is at a high latitude the impact of the earth's rotation on internal wave motions is not negligible. Both Poincaré and Kelvin waves, forms of rotationally modified gravity waves, were observed in the simulations. This was seen as a clockwise rotation of the horizontal velocity field (Poincaré waves) and a counterclockwise propagation of the internal waves with their crests and troughs being largest along the lake boundary (Kelvin waves). Both the rotating wave induced velocities and large nearshore wave amplitudes could potentially cause an increase in shear stress at the bed and therefore lead to higher rates of sediment resuspension. Therefore, incorporating the earth's rotation into even small hydrodynamic models is necessary for an accurate representation of the internal waves and subsequent circulations. In summary the internal waves and circulation in BML are far from linear and display complex patterns that are strongly influenced by rotation.

Chapter 6

Conclusions

6.1 Summary

The aim of this research was to provide the first description of the wind and internal waves in Base Mine Lake through field measurements, laboratory experiments, and numerical simulations. The goal is that this initial picture will help elucidate the impact of wave dependent mixing mechanisms on the water cap physics and subsequently inform reclamation decisions. Of particular interest in this study was the consequence of wave generated bottom orbital velocities on the resuspension of FFT and the effect of surface hydrocarbons on wind wave formation and growth.

In Chapter 2 the first ever measurements of surface wind waves on BML were presented. The data was collected using two subsurface pressure gauges set up at the northeast end of BML after fall turnover in 2015 and 2016. Post deployment the subsurface pressures were transformed into surface wind wave amplitudes through the application of linear wave theory. However, due to the short period of the wind waves on BML and the fact that wave properties, such as pressure, decay exponentially with depth, a large amount of measured wave energy existed at frequencies contaminated by noise. Therefore, a cutoff frequency acting as a low pass filter was necessary to avoid the overamplification of noise which would lead to an overestimation of surface wind wave amplitudes. A general procedure for deriving wave amplitudes from subsurface pressures is as follows:

1. Find the dynamic pressure signal by removing the atmospheric and hydrostatic pressure components from the raw signal.

2. Calculate the dynamic pressure spectrum by splitting the data into segments of equal length and applying a fast Fourier transform to each window.

3. Determine the linear wave theory transfer function, identical across windows if the segment length is equal, and apply it to the spectral estimate of dynamic pressure in each window. This results in a spectral estimate of the

surface elevation.

4. Define a cutoff frequency in which to apply a low-pass filter. In Jones and Monismith (2007) the suggested cutoff frequency is 12 times the noise floor. The study at hand chose the cutoff frequency as the frequency of a wave that has exponentially decayed by a factor of 5 at the sensor face.

5. Map the surface elevation spectrum into a surface elevation time series by performing an inverse fast Fourier transform.

The data presented in Chapter 2 revealed that significant wave heights in BML were as large as 40 cm during wind events. Additionally, as the wind waves propagate across the lake in a matter of minutes there is little ramp up or down time associated with a storm. Lastly, for preceding reasons, the choice of sensor sampling frequency and deployment depth is dependent on the waves of interest and in some cases multiple sensors deployed at various depths may be necessary.

Chapter 3 attempted to simulate the observed wind waves in BML using the SWAN model. In addition, the modeled bottom orbital velocities were used to determine the potential for resuspension of FFT. The model was calibrated over a three week period in 2015 and validated to observations of the surface wind waves during a 2 month period in 2016. In general, the predicted significant wave heights were coincident with and of the same magnitude as the observed wave heights. However, the model invariably overestimated wave heights when the observations dropped below 10 cm. It is thought that this could be attributed to inaccuracies in the input winds, numerical challenges of simulating high frequency waves, or potentially the dampening of small waves due to hydrocarbons on BML. The latter would mean that, because SWAN does not incorporate hydrocarbons, the estimates of small amplitude waves would not be dampened and therefore be larger than the observations.

Given the small surface area of BML the waves present, outside the immediate shoreline, are typically deep-water waves and therefore do not feel the bottom. It was shown that both the simulated and observed bottom orbital velocities rarely reach the critical value needed for resuspension of FFT. Even in the 10 year wind event the wave heights are so limited by the fetch of the lake that the corresponding bottom orbital velocities do not cause significant resuspension. In fact this finding is driven home further by the point that FFT is generally concentrated in deeper areas (>4 m) of the lake.

In Chapter 4 the effects of hydrocarbons on wind waves in BML were examined in the laboratory and field. This chapter is, to the best of my knowledge, the first attempt to quantify the impact of hydrocarbons on wind waves in a mine pit lake. It is also one of only a few studies to examine the impact of hydrocarbons on wind waves using both laboratory and field methods. The observed damping of high frequency waves, known as capillary waves, in the presence of an oil film, olive oil in the laboratory and hydrocarbons in the field, suggested that the net flux of momentum across the air water interface in BML is diminished. Additionally, since capillary waves are necessary for the development of gravity waves it is expected that the gravity wave field in BML takes more time to develop and grows at a slower rate. These findings are made more robust by the similarities of the laboratory and field results. In both cases the waves being dampened were near the wavelength at which the minimum phase speed occurs ($\approx$1.7 cm) and where the restoring forces of surface tension and gravity are equivalent. This work helps to explain the observed differences in the wave field between BML and a water body without a hydrocarbon film.

Lastly, Chapter 5 simulated the internal waves in BML using Delft3D Flow. The simulations were performed during summer stratification and spanned a 4 day period. Results of the simulations at 3 thermistor chains in BML accurately matched the phase and in most cases the amplitude of the observed internal waves. However, the model consistently underestimated the wave crests at platform 2 and deviated from the observed amplitudes at all stations with the addition of time. Contrary to most 3D simulations of internal waves a non-uniform wind drag coefficient was implemented and based off observations from BML. It was found that this had a non-negligible impact on the mixed layer depth and hence the internal wave amplitudes. Perhaps the most stunning finding of this chapter was the impact of the earth's rotation on the internal waves in a small lake such as BML. Without the incorporation of the Coriolis force the model produced wrongful estimates of the wave amplitudes throughout the domain, but especially along the boundaries of the lake. With the Coriolis force the simulated internal waves took the form of Poincaré and Kelvin waves. It is likely that these rotationally modified gravity waves not only complicate the lake circulation, but lead to increased rates of mixing throughout the lake.

6.2 Impacts on Reclamation

The impacts of surface and internal waves on a lakes physical processes are significant. They cause sediment resuspension and transport, mixing across the thermocline and air-water interface, and drive local and lake wide circulation among other things. Within BML high levels of turbidity throughout the water column and near the bed, along with anoxic like conditions during stratification, present major challenges for reclamation. A short list summarizing the potential consequences of waves to reclamation is as follows:

1. Given the small amplitudes of the surface waves on BML it is unlikely that they cause resuspension of FFT. In fact most of the lake during a majority of the time will not feel the surface waves at all due to the complete decay of wave properties before the bed.

2. The internal waves in BML are on the order of meters and therefore quite possibly create circulation patterns and near bed orbital velocities that are capable of resuspending FFT.

3. Surface waves are important in driving the flux of gases, such as oxygen, across the air-water interface. Therefore, the dampening of wind waves by hydrocarbons is likely affecting the oxygen concentration in the epilimnion and subsequently the hypolimnion.

4. The internal waves in BML are rotationally modified and therefore take the form of Poincaré and Kelvin waves. In the case of Kelvin waves there is potential for subsurface wave breaking and upwelling and downwelling in the nearshore areas of BML. This could lead to increases in turbidity and potentially resuspension of nearshore FFT.

6.3 Future Work

The findings presented in this thesis have created a strong first description of the surface and internal waves in Base Mine Lake. However, a number of improvements to the current work should be made in order to further our understanding of the wave processes. In addition the findings have raised new research questions that could motivate future research directions.

As this was the first attempt to measure the surface wind waves in BML a few changes to the field design could be made. First, a more complete

picture of the wind wave field could be achieved by deploying instruments at both ends of the lake. Additionally, instrumentation capable of resolving wave direction, such as Acoustic Doppler Current Profilers and Acoustic Doppler Velocimeters, should be considered. As a consequence of the decay of deep-water wave properties with depth a single pressure sensor is not capable of resolving the entire wave field. Therefore, future setups should include multiple pressure sensors sampling in the same location but at varying depths.

It was found that SWAN consistently overestimated small wave heights. One reason could be that wind inputs from directions other than the west and southwest, the long fetch directions, are not an accurate representation of the wind present at the pressure sensors. This is likely because the pressure sensors are sheltered by the topography when the winds are from the northeast through south sectors. Instead a wind sensor mounted at the location of the pressure sensors would provide a more accurate wind field and help to determine if the model overestimation of small wave heights is due to inaccurate wind inputs. Another possibility for the overestimation is that SWAN does not account for reduced surface tension from hydrocarbons. Therefore, a parameterization of the hydrocarbons impact on wind waves could be implemented in SWAN. In general future work should focus on improving the model estimates of small wave heights by determining the reasons for the overestimation.

In the laboratory the effect of hydrocarbons on wind waves should be investigated further. Particularly the critical wind speed needed for wind wave generation should be determined. This would involve first creating an oil film and then testing a range of wind speeds. In addition, the effect of hydrocarbons on whitecapping and wave breaking should be examined as this impacts the fluxes of gas, heat, and momentum through the air-water interface. A more robust field experiment should be conducted using pressure sensors to measure high frequency waves in the presence and absence of hydrocarbons. Additionally, time-lapse photographs of the water's surface would help indicate when an oil sheen is present and assist in estimating the critical wind speed on BML. Lastly, there should also be some quantification of how thick the hydrocarbon layer is at the time of the measurements. This could be done using optical methods such as laser light absorption.

The internal waves in BML were simulated for 4 days. A longer simulation covering the entire period of stratification, approximately mid-May through August, should be performed. This would involve properly modelling the heat flux, coupling the waves, and better determining the values for vertical and horizontal eddy diffusivity and viscosity. One of the most

surprising findings of this study was the impact of the Coriolis force on internal waves. However, while the effect is apparent the impact that it has on lake circulation and water cap physics is still unclear. Future work to validate the simulated rotationally modified gravity waves and their subsequent circulation to field observations is needed. A coupling of the waves, flow, and potentially biology and sediment transport modules of Delft3D could provide crucial insight into the structure and cycling of BML.

Bibliography

J. Aitken. 3. on the effect of oil on a stormy sea. *Proceedings of the Royal Society of Edinburgh*, 12:56–75, 1884.

P. Behroozi, K. Cordray, W. Griffin, and F. Behroozi. The calming effect of oil on water. *American Journal of Physics*, 75(5):407–414, 2007.

D. Beletsky, W. P. OConnor, D. J. Schwab, and D. E. Dietrich. Numerical simulation of internal kelvin waves and coastal upwelling fronts. *Journal of Physical oceanography*, 27(7):1197–1215, 1997.

C. T. Bishop and M. A. Donelan. Measuring waves with pressure transducers. *Coastal Engineering*, 11(4):309–328, 1987.

N. Booij, R. Ris, and L. H. Holthuijsen. A third-generation wave model for coastal regions: 1. model description and validation. *Journal of geophysical research: Oceans*, 104(C4):7649–7666, 1999.

J. V. Boussinesq. Théorie générale des mouvements qui sont propagés dans un canal rectangulaire horizontal. *CR Acad. Sci. Paris*, 73:256–260, 1871.

C. Bretschneider and R. Reid. Change in wave height due to bottom friction, percolation and refraction. In *34 th Annual Meeting of American Geophisical union*, 1954.

H. C. Broecker. The influence of wind on co_2-exchange in a wind-wave tunnel, including the effect of monolayers. *J. mar. Res.*, 36:595–610, 1978.

CEMA. Cumulative environmental management association: End pit lakes guidance document. 2012 (retrieved August 3, 2017). URL `http://www.cemaonline.ca`.

COSIA. Canada's oil sands innovation alliance: Guidelines for performance management of oil sands fluid fline tailings deposits to meet closure commitments. 2014 (retrieved August 3, 2017). URL `http://www.cosia.ca`.

D. B. Creamer and J. A. Wright. Surface films and wind wave growth. *Journal of Geophysical Research: Oceans*, 97(C4):5221–5229, 1992.

Delft Hydraulics. Delft3d-flow user manual. *Delft, the Netherlands*, 2006.

P. Dissanayake, H. Hofmann, and F. Peeters. Simulation of internal waves and surface currents in lakes: comparison of results from two 3d models and field data. 2016.

K. A. Dompierre, S. Lee Barbour, R. L. North, S. K. Carey, and M. B. Lindsay. Chemical mass transport between fluid fine tailings and the overlying water cover of an oil sands end pit lake. *Water Resources Research*, 2017.

B. Franklin, W. Brownrigg, and M. Farish. Of the stilling of waves by means of oil. extracted from sundry letters between benjamin franklin, ll. dfrs william brownrigg, mdfrs and the reverend mr. farish. *Philosophical Transactions*, 64:445–460, 1774.

G. D. Fulford. Pouring holy oil on troubled waters. *Isis*, 59(2):198–199, 1968.

D. Gabriel and T. Hedges. Effects of currents on interpretation of sub-surface pressure spectra. *Coastal engineering*, 10(4):309–323, 1986.

C. Giles. Franklins teaspoonful of oil. studies in the early history of surface chemistry, part 1. *Chemistry and Industry*, 1969.

R. M. Gorman and C. G. Neilson. Modelling shallow water wave generation and transformation in an intertidal estuary. *Coastal Engineering*, 36(3): 197–217, 1999.

Government of Alberta. Alberta energy: Our business, 2016 (retrieved August 3, 2017). URL `http://www.energy.alberta.ca/oilsands`.

K. Hasselmann, T. Barnett, E. Bouws, H. Carlson, D. Cartwright, K. Enke, J. Ewing, H. Gienapp, D. Hasselmann, P. Kruseman, et al. Measurements of wind-wave growth and swell decay during the joint north sea wave project (jonswap). Technical report, Deutches Hydrographisches Institut, 1973.

B. R. Hodges, J. Imberger, A. Saggio, and K. B. Winters. Modeling basin-scale internal waves in a stratified lake. *Limnology and oceanography*, 45 (7):1603–1620, 2000.

R. Hoeke, C. Storlazzi, and P. Ridd. Hydrodynamics of a bathymetrically complex fringing coral reef embayment: Wave climate, in situ observations, and wave prediction. *Journal of Geophysical Research: Oceans*, 116 (C4), 2011.

K.-R. Jin and Z.-G. Ji. Calibration and verification of a spectral wind–wave model for lake okeechobee. *Ocean Engineering*, 28(5):571–584, 2001.

N. L. Jones and S. G. Monismith. Measuring short-period wind waves in a tidally forced environment with a subsurface pressure gauge. *Limnol. Oceanogr. Methods*, 5:317–327, 2007.

S. Kawai. Discussion on the critical wind speed for wind-wave generation on the basis of shear-flow instability theory. *Journal of the Oceanographical Society Japan*, 35(2):179–186, 1979.

B. Kinsman. *Wind waves: their generation and propagation on the ocean surface*. Courier Corporation, 1965.

G. Lawrence, P. Ward, and M. MacKinnon. Wind-wave-induced suspension of mine tailings in disposal ponds–a case study. *Canadian Journal of Civil Engineering*, 18(6):1047–1053, 1991.

G. A. Lawrence, E. W. Tedford, and R. Pieters. Suspended solids in an end pit lake: potential mixing mechanisms. *Canadian Journal of Civil Engineering*, 43(3):211–217, 2016.

B. D. LaZerte. The dominating higher order vertical modes of the internal seiche in a small lake. 1980.

B. Le Méhauté and R. C. Koh. On the breaking of waves arriving at an angle to the shore. *Journal of Hydraulic Research*, 5(1):67–88, 1967.

A. K. Liu, Y. S. Chang, M.-K. Hsu, and N. K. Liang. Evolution of nonlinear internal waves in the east and south china seas. *Journal of Geophysical Research: Oceans*, 103(C4):7995–8008, 1998.

H.-T. Liu and J.-T. Lin. Effects of an oil slick on wind waves 1. In *International Oil Spill Conference*, volume 1979, pages 665–674. American Petroleum Institute, 1979.

R. J. Lowe, J. L. Falter, M. D. Bandet, G. Pawlak, M. J. Atkinson, S. G. Monismith, and J. R. Koseff. Spectral wave dissipation over a barrier reef. *Journal of Geophysical Research: Oceans*, 110(C4), 2005.

E. Lucassen-Reynders and J. Lucassen. Properties of capillary waves. *Advances in colloid and interface science*, 2(4):347–395, 1970.

P. J. Martin. Simulation of the mixed layer at ows november and papa with several models. *Journal of Geophysical Research: Oceans*, 90(C1): 903–916, 1985.

G. L. Mellor and T. Yamada. A hierarchy of turbulence closure models for planetary boundary layers. *Journal of the Atmospheric Sciences*, 31(7): 1791–1806, 1974.

G. L. Mellor and T. Yamada. Development of a turbulence closure model for geophysical fluid problems. *Reviews of Geophysics*, 20(4):851–875, 1982.

S. Monismith. Modal response of reservoirs to wind stress. *Journal of Hydraulic Engineering*, 113(10):1290–1304, 1987.

C. H. Mortimer. Water movements in lakes during summer stratification; evidence from the distribution of temperature in windermere. *Philosophical Transactions of the Royal Society of London B: Biological Sciences*, 236(635):355–398, 1952.

D. Mowbray and B. Rarity. A theoretical and experimental investigation of the phase configuration of internal waves of small amplitude in a density stratified liquid. *Journal of Fluid Mechanics*, 28(1):1–16, 1967.

K. L. Oliveras, V. Vasan, B. Deconinck, and D. Henderson. Recovering the water-wave profile from pressure measurements. *SIAM Journal on Applied Mathematics*, 72(3):897–918, 2012.

Y. Ozeren and D. Wren. Technical note: Predicting wind-driven waves in small reservoirs. *Transactions of the ASAE (American Society of Agricultural Engineers)*, 52(4):1213, 2009.

A. Pannard, B. E. Beisner, D. F. Bird, J. Braun, D. Planas, and M. Bormans. Recurrent internal waves in a small lake: Potential ecological consequences for metalimnetic phytoplankton populations. *Limnology and Oceanography: Fluids and Environments*, 1(1):91–109, 2011.

R. Pieters and G. A. Lawrence. Physical processes and meromixis in pit lakes subject to ice cover. *Canadian Journal of Civil Engineering*, 41(6): 569–578, 2014.

A. Pockels. Relations between the surface tension and relative contamination of water surfaces. *Nature*, 48:152, 1893.

O. Reynolds. On the effect of oil in destroying waves on the surface of water. *Brit. Assoc. Rept. Papers*, 50:489–490, 1880.

D. J. Schwab, J. R. Bennett, P. C. Liu, and M. A. Donelan. Application of a simple numerical wave prediction model to lake erie. *Journal of Geophysical Research: Oceans*, 89(C3):3586–3592, 1984.

C. Seibt, F. Peeters, M. Graf, M. Sprenger, and H. Hofmann. Modeling wind waves and wave exposure of nearshore zones in medium-sized lakes. *Limnology and Oceanography*, 58(1):23–36, 2013.

B. Sparrow. Annual report of the united states life-saving service. *Reports of Comittees*, 427(1), 1883.

C. L. Stevens and G. A. Lawrence. Estimation of wind-forced internal seiche amplitudes in lakes and reservoirs, with data from british columbia, canada. *Aquatic Sciences-Research Across Boundaries*, 59(2):115–134, 1997.

A. Stigebrandt. Vertical diffusion driven by internal waves in a sill fjord. *Journal of Physical Oceanography*, 6(4):486–495, 1976.

G. G. Stokes. On the theory of oscillatory waves. *Trans Cambridge Philos Soc*, 8:441–473, 1847.

O. P. Strausz and E. M. Lown. *The chemistry of Alberta oil sands, bitumens and heavy oils*. Alberta Energy Research Institute Calgary, Alberta, Canada, 2003.

Suncor. Process, 2016 (retrieved August 3, 2017). URL `http://www.suncor.com`.

H. U. Sverdrup and W. H. Munk. Wind, sea, and swell: theory of relations for forecasting. 1947.

SWAN Team et al. swan cycle iii, version 40.85: Scientific and technical documentation. *Delft, The Netherlands: Delft University of Technology, digital version available in http://www. fluidmechanics. tudelft. nl/swan/index. htm*, 2011.

H. L. Tolman and D. Chalikov. Source terms in a third-generation wind wave model. *Journal of Physical Oceanography*, 26(11):2497–2518, 1996.

M. Townsend and J. D. Fenton. A comparison of analysis methods for wave pressure data. pages 575–588, 1997.

C.-H. Tsai, F.-J. Young, Y.-C. Lin, and H.-W. Li. Comparison of methods for recovering surface waves from pressure transducers. In *Ocean Wave Measurement and Analysis (2001)*, pages 347–356. 2002.

C.-H. Tsai, M.-C. Huang, F.-J. Young, Y.-C. Lin, and H.-W. Li. On the recovery of surface wave by pressure transfer function. *Ocean Engineering*, 32(10):1247–1259, 2005.

U. A. C. o. E. USACE. Shore protection manual. *Coastal Engineering Research Center, Vicksburg, MS.*, 1, 1984.

H. Wang, D.-Y. Lee, and A. Garcia. Time series surface-wave recovery from pressure gage. *Coastal engineering*, 10(4):379–393, 1986.

R. Wetzel. *Limnology*. Saunders Company, 1983.

P. L. Wiberg and C. R. Sherwood. Calculating wave-generated bottom orbital velocities from surface-wave parameters. *Computers & Geosciences*, 34(10):1243–1262, 2008.

R. Wiegel. A presentation of cnoidal wave theory for practical application. *Journal of Fluid Mechanics*, 7(2):273–286, 1960.

C. J. Willmott. Some comments on the evaluation of model performance. *Bulletin of the American Meteorological Society*, 63(11):1309–1313, 1982.

A. Wüest and A. Lorke. Small-scale hydrodynamics in lakes. *Annual Review of fluid mechanics*, 35(1):373–412, 2003.

Appendices

Appendix A

The wind speed and direction recorded at Sandhill Fen Site 3 was compared with the values recorded at the BML Central Platform during a one year period (Figure A.1). In general the wind speed at Sandhill Fen Site 3 is representative of the wind speed at the BML Central Platform (Figure A.1A). However, at high wind speeds the Central Platform values are greater than the Sandhill Fen values. This is likely because the Central Platform is over water and therefore the wind drag coefficient, C_d, is reduced. The wind direction at the Sandhill Fen also agrees well with the wind direction at the Central Platform during much of the year (Figure A.1B).

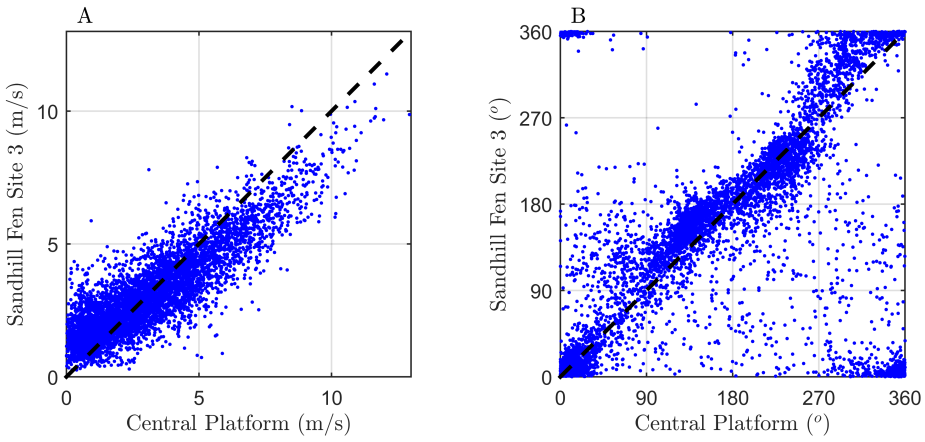

Figure A.1: Comparison of the wind speed (A) and direction (B) recorded at Sandhill Fen Site 3 and the BML Central Platform. The dashed line represents the 1:1 ratio. Notice that a direction of 360^o is identical to a direction of zero.

To get an understanding of the direction that the wind speed came from

during the 2015 and 2016 sampling periods a compass plot is shown in Figure A.2. During both sampling periods the wind was primarily out of either the Southwest, Southeast, or North (Figure A.2A,C). Furthermore, wind speeds in excess of 5 m/s were largely from the Southwest through North sector. This is inline with the long fetch of BML.

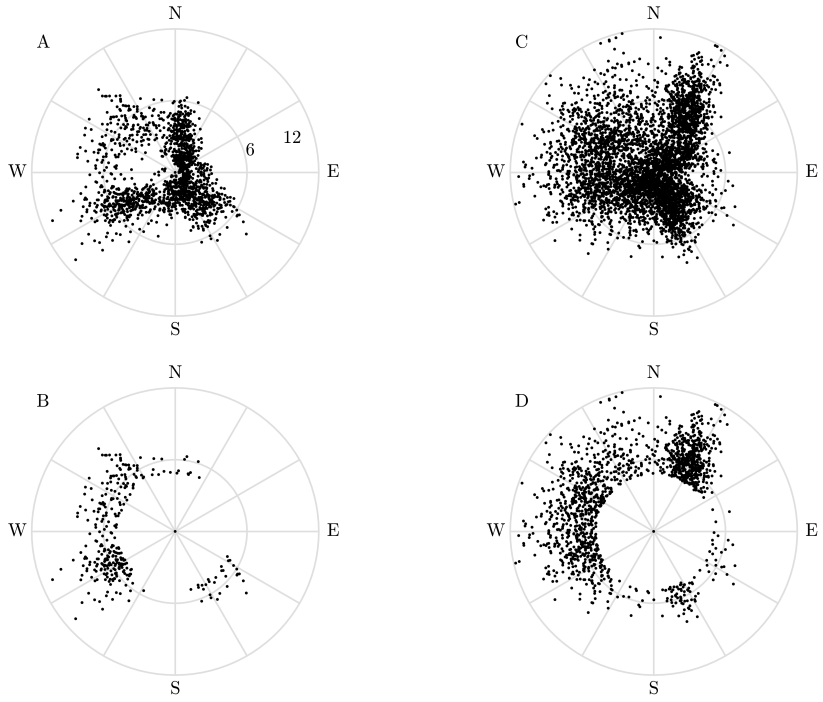

Figure A.2: The observed hourly average wind direction and speed at Sandhill Fen Site 3 for the 2015 and 2016 campaigns. The total record for the 2015 (A) and 2016 (C) campaigns along with winds greater than 5 m/s for 2015 (B) and 2016 (D). The inner radius represents 6 m/s and the outer represents 12 m/s. The wind direction is the direction in which the wind is from.

Appendix B

Table B.1: SWAN model parameters after calibration to the 2015 observed wave heights.

Model Parameters	Parameter Value
# Frequency Bins	72
Min Frequency	0.25 Hz
Max Frequency	3 Hz
# Direction Bins	36
Direction Range	360^o
Density of Water	1001 kg/m^3
Depth Induce Breaking	True
Breaking Alpha	1.00
Breaking Gamma	0.73
Bed Friction Type	JONSWAP
Bed Friction Coefficient	0.067 m^2/s^3
Diffraction	True
Diffraction Coefficient	0.15
Whitecapping	Komen
Wave-wave Interactions	True
Refraction	True
Wave Energy Dissipation	3D

Table B.2: Delft3D Flow model parameters.

Model Parameters	Parameter Value
Latitude	58^o N
Δt	30 s
# Z layers	20
Density of Water	1001 kg/m^3
Air Density	1 kg/m^3
Salinity	31 ppt
C_d (0-1.75 m/s)	0.04
C_d (1.75-5 m/s)	0.002
C_d (5+ m/s)	0.0012
Chezy Roughness (U/V)	130
Slip Condition	Free
Horizontal Eddy Viscosity	0.01 m^2/s
Horizontal Eddy Diffusivity	0.01 m^2/s
Vertical Eddy Viscosity	0.00 m^2/s
Vertical Eddy Diffusivity	0.00 m^2/s
Turbulent Closure Scheme	k-ϵ
Heat Flux	None

Appendix C

This script converts a time series of absolute subsurface pressure (p) into a time series of surface elevation (η) following the procedures layed out in Chapter 2, Jones and Monismith (2007), and Wiberg and Sherwood (2008). All variables in the code are inline with the variables presented in the thesis. The script should only be used for deep-water waves as it calculates the pressure transfer function (K_z) using the deep-water wavenumber ($(4pi^2)(gT^2)^{-1}$). Along with surface elevation the following variables are output:

H_s	Significant wave height
Tm_{02}	Average zero crossing period
Tm_{01}	Mean wave period
U_b	Bottom orbital velocity

```
%% ##################### HEADER #########################
%
% DISCLAIMER:
%   The following code is provided
%   "as is" with no assurance of its accuracy,
%   effeciency, or use in any circumstance.
%
%   Additionally, while this code makes processing
%   subsurface pressure signals to surface elevation
%   signals easier it still requires at least a basic
%   understanding of linear wave theory and a working
%   knowledge of the instrument (ie. understanding
%   deep water vs. shallow water waves).
%
%*************************************************
%
% FILENAME: Press2Waves.m
%
% AUTHOR:   David Hurley
% CREATED:  July 31, 2017
% CONTACT:  dlhurley@ncsu.edu
%
%*************************************************
%
```

```
25 % DESCRIPTION:
26 %       Converts an absolute pressure signal into a
27 %       surface elevation signal and computes
28 %       corresponding oceanographic variables.
29 %
30 % INPUT PARAMETERS:
31 %       p:          Absolute pressure (dbar)
32 %       pa:         Atmospheric pressure (dbar)
33 %       rho:        Density of water (kg/m^3)
34 %       g:          Gravitational acceleration (m/s^2)
35 %       z:          Depth of instrument (m, negative down)
36 %       Fs:         Instrument sampling rate (Hz)
37 %       Fc:         Cutoff frequency (Hz)
38 %       d:          Water depth at instrument (m)
39 %       N:          # of samples in moving window
40 %                   (Fs = 16Hz then N = 9600 is 10 min)
41 %
42 % OUTPUT PARAMETERS:
43 %       pd:         Dynamic Pressure (m)
44 %       Eta:        Surface elevation signal (m)
45 %       Hs:         Significant wave height (m)
46 %       Tm02:       Average zero crossing wave period (s)
47 %       Tm01:       Mean wave period (s)
48 %       Ubr:        Bottom orbital velocity (m/s)
49 %
50 % REFERENCES:
51 %       1) D. Hurley. Wind waves and internal waves in
52 %       Base Mine Lake. University of British Columbia,
53 %       2017.
54 %
55 %       2) N. Jones and S. Monismith. Measuring short-
56 %       period wind waves in a tidally forced
57 %       environment with a subsurface pressure gauge.
58 %       Limnology and Oceanography Methods, 5:317-327,
59 %       2007.
60 %
61 %       3) P. Wiberg and C. Sherwood. Calculating wave-
62 %       generated bottom orbital velocities from
63 %       surface-wave parameters. Computers &
64 %       Geosciences, 34(10):1243-1259, 2005.
```

```
65 %
66 % ###################### HEADER END ##################
67
68 %% ###################### SCRIPT START ###############
69
70 clear;
71 close;
72
73 load Inputs
74
75 % 1) Convert absolute pressure to gauge pressure
76 pg = p - pa;
77
78 % 2) Convert gauge pressure to dynamic pressure
79 %    by removing hydrostatic pressure.
80 %    *** change dbar ---> meters of water ***.
81 pd = (pg.*10000) / (rho*g) + z;
82
83 % 3) Create frequency vector for fast Fourier
       transform.
84 F = Fs*[0:1/(N-1):1]';
85
86 % 4) Calculate pressure transfer function.
87 Kz = cosh((4*pi^2)./(g*(1./F).^2)* ...
88      (z+d))./cosh((4*pi^2)./(g*(1./F).^2)*d);
89
90 Kz(find(isnan(Kz)==1))=0;              % NaN == 0
91 Kz = [Kz(1:N/2);Kz(N/2:-1:1)];        % Mirror Kz
92
93 % 5) Calculate surface elevation signal and
94 %    oceanographic parameters.
95 for i = 1:N:length(p)-(N+1)
96
97     % Dynamic pressure spectrum
98     Spd = fft(pd(i:i+(N-1)));
99
100    % Surface elevation spectrum
101    Seta = Spd./Kz;
102
103    % Make all energy above cutoff frequency zero
```

```
104     Seta(find(F>Fc & F<Fs-Fc)) = 0;
105
106     % Convert surface elevation spectrum into surface
107     % elevation time signal
108     Eta{i} = real(ifft(Seta));
109
110     % Calculate spectral moments
111     % (Jones and Monismith (2007))
112     M0 = sum(2*abs(Seta(1:N/2)).^2 )./N^2;
113     M1 = sum(2*F(1:N/2).*abs(Seta(1:N/2)).^2)./N^2;
114     M2 = sum(2*F(1:N/2).^2.*abs(Seta(1:N/2)).^2)./N^2;
115
116     % Calculate significant wave height
117     % (Shore Protection Manual (1984))
118     Hs{i} = 4*(M0)^0.5;
119
120     % Calculate wave periods (SWAN User Manual (2011))
121     Tm01{i} = M0/M1;
122     Tm02{i} = (M0/M2)^0.5;
123
124     % Calculate bottom orbital velocity
125     % (Wiberg and Sherwood (2008))
126     Ubr{i} = (2*nansum(((4*pi^2)./((1./F(1:N/2))...
127         .^2.*sinh(((4*pi^2)./(g.*(1./F(1:N/2)).^2))...
128         .*d).^2)).*2.*abs(Seta(1:N/2)).^2)./N^2).^0.5;
129 end
130
131 % 6) Concatenate output parameters
132 Eta  = cat(1,Eta{:});
133 Hs   = cat(1,Hs{:});
134 Tm01 = cat(1,Tm01{:});
135 Tm02 = cat(1,Tm02{:});
136 Ubr  = cat(1,Ubr{:});
137
138 save Output Eta Hs Tm01 Tm02 Ubr pd
139
140 %% ##################### END ######################
```